

Temperature transformation recovering the compressible law of the wall for turbulent channel flow

Youjie Xu,^{1,*} Steffen J. Schmidt,¹ and Nikolaus A. Adams^{1,2}

¹*Chair of Aerodynamics and Fluid Mechanics,*

TUM School of Engineering and Design, Technical University of Munich,

BoltzmannstraSSe 15, 85748 Garching, Germany

²*Munich Institute of Integrated Materials,*

Energy and Process Engineering, Technical University of Munich,

LichtenbergstraSSe 4a, 85748 Garching, Germany

(Dated: November 11, 2025)

Abstract

Velocity and temperature distribution are both crucial for modeling compressible wall-bounded turbulent flows. The compressible law of the wall for velocity has been extensively examined through velocity transformations. However, the issue of a well-established temperature transformation remains open. We propose a new temperature transformation for compressible turbulent channel flow. Our approach is based on the analysis of momentum and energy balance equations in the overlap layer. It accounts for the influences of mixing length model, the work of the body force, and the turbulent kinetic energy transport. Two types of temperature transformations are obtained: Van Driest type (VD-type) and semi-local type (SL-type). The performance of these transformations is evaluated using data from direct numerical simulations and wall-resolved large eddy simulations of compressible turbulent channel flow. Both the VD-type and SL-type transformations apply to isothermal and adiabatic walls. The SL-type transformation provides better data collapse in the viscous sublayer and buffer layer, thereby recovering the temperature law of the wall. When a suitable mixing length model is applied, the SL-type transformation yields results that agree with the incompressible temperature profile or exhibit extended logarithmic behavior. Results from the present study highlight careful consideration of the turbulent kinetic energy transport term in different thermal boundary conditions. Applications of the proposed transformation in near-wall modeling and its potential extension to more general configurations are also discussed.

I. INTRODUCTION

Wall-bounded turbulent flow plays a crucial role in various applications, including aircraft aerodynamics [1, 2], atmospheric flows [3], wind farm optimization [4], etc. It is well known that, in high-Reynolds-number incompressible turbulent boundary layers, the mean streamwise velocity follows the law of the wall, typically expressed as [5]:

$$U^+ = \begin{cases} y^+, & \text{viscous sublayer,} \\ \frac{1}{\kappa} \ln(y^+) + B, & \text{logarithmic layer.} \end{cases} \quad (1)$$

Here, $U^+ = \bar{u}/u_\tau$, $u_\tau = \sqrt{\tau_w/\bar{\rho}_w}$, and $y^+ = \bar{\rho}_w u_\tau y / \bar{\mu}_w$, where τ_w , $\bar{\rho}_w$, and $\bar{\mu}_w$ are the mean shear stress, density, and dynamic viscosity at the wall, respectively. κ represents the von Kármán constant, and B is an integration constant.

* youjie.xu@tum.de

Reynolds analogy suggests that heat and momentum transfer exhibit similar behavior when the Prandtl number approaches unity. The underlying logic is that fluid motions transport the momentum and heat flux simultaneously [6]. This implies the existence of the law of the wall for temperature above non-adiabatic wall, expressed as [7, 8]:

$$T^+ = \begin{cases} Pr y^+, & \text{viscous sublayer,} \\ \frac{Pr_t}{\kappa} \ln(y^+) + B_T, & \text{logarithmic layer.} \end{cases} \quad (2)$$

Here, $T^+ = (\bar{T} - \bar{T}_w)/T_\tau$, and $T_\tau = q_w/(\bar{\rho}_w c_p u_\tau)$. The terms \bar{T}_w and q_w represent the wall temperature and heat flux removed from the wall. $\bar{\rho}_w$ and u_τ retain their definitions from Eq. (1). Pr and Pr_t denote the molecular and turbulent Prandtl number. B_T is the counterpart of B in Eq. (1) and typically depends on Pr .

Eqs.(1) and (2) are applicable to incompressible flows. Many existing studies support the law of the wall for velocity distribution [9–11] and temperature distribution [12–16]. However, their accuracy decrease with increasing Mach number due to aerodynamic heating effects and the coupling between velocity and temperature fields. According to Morkovin [17], the difference between compressible and incompressible turbulence for moderate Mach numbers can be accounted for by taking into consideration of variations in fluid properties. Based on this idea, numerous velocity transformations have been established to transform the compressible turbulent velocity profile into its incompressible counterpart [18–26], thereby validating the compressible law of the wall for velocity.

In order to describe the temperature profile in compressible boundary layers, two primary strategies have been explored in the literature. The first one involves developing a temperature-velocity relation (TV-relation), where the mean temperature is expressed as a function of the mean velocity. The second strategy focuses on establishing a temperature transformation, analogous to the idea of velocity transformation.

Examples of TV-relation include the formulations from the last century [27–29] and recent developments [30–32]. These relations are built upon the Strong Reynolds Analogy [17] and exhibit good performance across a wide range of flows [33, 34]. However, these relations require the velocity and temperature at the boundary layer edge as input [33, 35, 36]. For internal flows, such as compressible turbulent channel and pipe flows, the centerline velocity and temperature are not known *a priori*. Regarding this issue, Song *et al.* [37] proposed an approach to determine the centerline temperature for turbulent channel and pipe flows. However, this method is limited to

the classical isothermal wall configuration. For more complex configurations, such as compressible turbulent channel flows with mixed isothermal/adiabatic wall conditions [38], the TV-relation encounters several challenges. First, it is often difficult to determine the boundary layer edge [35], as the mean flow field is no longer symmetry about the centerline. In Lusher and Coleman [38] and Huang *et al.* [8], the boundary layer edge is defined as the location where the mean velocity approaches its maximum value. But it remains unclear whether this position can be regarded as the thermal boundary layer edge. Second, neither the centerline temperature nor the temperature at the position of maximum velocity can be predicted by the approach of Song *et al.* [37]. More importantly, even when these temperatures are available, applying them in the commonly used TV-relations still leads to noticeable discrepancies, which can be validated using the DNS data of Lusher and Coleman [38].

In contrast to the TV-relation, the temperature transformation is formulated through an incremental wall-normal integration without relying on velocity and temperature values at the boundary layer edge. The resulting formulation is consistent with the classical law of the wall [39]. However, such a temperature scaling law has not been well established. Preliminary results for this strategy have been reported in several studies [8, 20, 35, 40–43].

A straightforward approach to construct a temperature transformation for compressible turbulent flows is to follow the philosophy of VD-type velocity transformation [18]. For example, Brun *et al.* [20] derived a VD-type transformation of the total temperature expressed as $\tilde{T}_{i,VD}^+ = \int_0^{\tilde{T}_i^+} \sqrt{\bar{\rho}/\bar{\rho}_w} d\tilde{T}_i^+ = \frac{Pr_t}{\kappa} \log (y^+) + B_T$. However, it does not collapse the buffer layer very well. To address this, they further proposed an integral length scaling and corresponding integral temperature transformation, which account for variation in both density and dynamic viscosity. This transformation reduces the scatter of the intercept significantly, leading to better agreement with experimental values.

Patel *et al.* [41] investigated flows over non-adiabatic walls under low-Mach-number conditions and proposed an extended VD-type temperature transformation. Their results demonstrate a good collapse of the transformed temperature profile. More recently, Modesti and Pirozzoli [43] developed a temperature transformation that accounts for variable fluid properties under low-Mach-number conditions. However, since aerodynamic heating was not considered in both studies, the performance of these transformations in compressible flows cannot be guaranteed. Furthermore, they encounter a singularity issue when applied to adiabatic wall boundary conditions. To address this problem, Chen *et al.* [42] proposed using local heat flux instead of wall heat flux, which

leads to unified temperature transformations applicable to both isothermal and adiabatic walls. It is worth noting that high-order statistics, especially the turbulent kinetic energy (TKE) transport term, is retained in the local heat flux, which improves the performance of their transformations.

Huang *et al.* [8] proposed VD-type and SL-type temperature transformations, which apply to both isothermal and adiabatic wall conditions, with the SL-type transformation showing superior performance. More recently, Cheng and Fu [35] proposed three Mach number invariant functions and a new SL-type transformation that demonstrates good performance above adiabatic wall in turbulent channel flow and isothermal wall in turbulent boundary layer flow.

The studies of Chen *et al.* [42], Huang *et al.* [8], and Cheng and Fu [35] demonstrate the possibility of recovering the temperature law of the wall in compressible turbulent flows. The most important lesson of their studies is that variations in fluid properties and aerodynamic heating effects should be taken into consideration. Incorporating the effect of high-order statistics can also enhance the performance of the transformation. However, it should be noted that there is still room for improvement in previous transformations. For instance, the slope of the logarithmic profile remains unsatisfactory in the results of Chen *et al.* [42]. At relatively low Reynolds numbers, the logarithmic profile under the transformation by Huang *et al.* [8] is less pronounced. The transformation by Cheng and Fu [35] is effective for adiabatic wall in turbulent channel flow, but its performance is less satisfactory for isothermal walls.

Considering the Reynolds analogy, the log-law for temperature and velocity distribution would share the same fundamental arguments. The log-law for velocity is supported by the arguments of Prandtl and Millikan [44]. Prandtl's reasoning relies on the assumptions of linear variation of mixing length ($l_m = \kappa y$) and uniform (constant) shear stress in the near wall region. Millikan's argument is based on asymptotic matching of the law of the wall in the inner layer and the velocity-defect law in the outer layer [5, 39, 44–46].

When focusing on compressible turbulent channel flow, there are three aspects that could be improved. First, it has been shown that the mixing length model $l_m = \kappa y$ is inaccurate, and the parabolic form $l_m = \kappa y \sqrt{1 - y/h}$ is a more suitable choice for turbulent channel flow [44]. Here, h is the half-channel height. Second, the assumption of constant shear stress in the logarithmic region is also problematic. The driving force (external body force or pressure gradient) and its work on the fluid should be considered in the energy equation. Third, the TKE transport, typically neglected in the transformations proposed by Huang *et al.* [8], could also be included, as demonstrated in the transformation by Chen *et al.* [42] and Cheng and Fu [35].

Given these limitations, we propose new VD-type and SL-type temperature transformations that account for the effects of mixing length model, body force, and the TKE transport. These transformations are applicable to both isothermal and adiabatic wall boundary conditions in compressible turbulent channel flow.

The paper is organized as follows: Sec. II gives the detailed derivation of the temperature transformation. Sec. III evaluates the performance of the proposed transformation. Sec. IV provides insights into the effect of the introduced parameters. Simplified forms of the transformations are provided. Applications of the transformation in near-wall modeling and its potential extension to more general flow configurations are discussed. Finally, concluding remarks are given in Sec. V.

II. COMPRESSIBLE LAW OF THE WALL FOR TEMPERATURE

Our derivation follows the general approach of Chen *et al.* [42] and Huang *et al.* [8], but it differs in three key differences. First, the transformation is defined based on the momentum and energy balance equations in the overlap layer, with an additional requirement imposed on the mixing length l_m to ensure consistency within the viscous sublayer. Second, we do not neglect the body force and its work on the fluid. Third, we account for the TKE transport in the energy balance equation. Considering these differences, we provide a complete derivation in this section for clarity and readability.

Throughout this study, x , y , and z denote the streamwise, wall-normal, and spanwise directions, with corresponding velocity components denoted by u , v and w . For generalization, u_i ($i = 1, 2, 3$) represents the velocity components. Reynolds averaging is expressed as $\phi = \bar{\phi} + \phi'$, whereas Favre averaging is given by $\phi = \tilde{\phi} + \phi''$, where $\tilde{\phi} = \overline{\rho\phi}/\bar{\rho}$. Quantities at the wall are denoted by the subscript w , while the superscripts $+$ and $*$ represent wall scaling and semi-local scaling. The subscripts VD and SL denote Van Driest type and semi-local type transformations.

A. Governing equations

For simplicity, we focus on compressible turbulent channel flow with periodic boundary conditions in streamwise and spanwise directions, and no-slip condition at the two walls. The governing equations for mass, momentum and energy conservations are:

$$\frac{\partial \rho}{\partial t} + \frac{\partial \rho u_j}{\partial x_j} = 0, \quad (3)$$

$$\frac{\partial \rho u_i}{\partial t} + \frac{\partial \rho u_j u_i}{\partial x_j} = -\frac{\partial p}{\partial x_i} + \frac{\partial \tau_{ij}}{\partial x_j} + f_x \delta_{i1}, \quad (4)$$

$$\frac{\partial}{\partial t} \left[\rho \left(c_v T + \frac{u_i u_i}{2} \right) \right] + \frac{\partial}{\partial x_j} \left[\left(\rho c_v T + \frac{\rho u_i u_i}{2} + p \right) u_j \right] = \frac{\partial \tau_{ij} u_i}{\partial x_j} - \frac{\partial q_i}{\partial x_i} + f_x u_1, \quad (5)$$

with the viscous stress τ_{ij} and heat flux vector q_i given by:

$$\tau_{ij} = \mu \left(\frac{\partial u_i}{\partial x_j} + \frac{\partial u_j}{\partial x_i} - \frac{2}{3} \delta_{ij} \frac{\partial u_k}{\partial x_k} \right), \quad q_i = -\lambda \frac{\partial T}{\partial x_i}. \quad (6)$$

Here, ρ, p, T represent density, pressure, temperature, respectively. μ and λ are the dynamic viscosity and molecular thermal conductivity. f_x is the external body force in streamwise direction. δ_{ij} denotes Kronecker delta notation. The ideal gas material model $p = \rho RT$ is used to close the governing equations, where R is gas constant. The specific heat capacities at constant volume and constant pressure are given by $c_v = R/(\gamma - 1)$ and $c_p = \gamma R/(\gamma - 1)$, respectively, where the specific heat ratio is $\gamma = 1.4$.

As pointed out by Huang *et al.* [47], the flow is driven by an external streamwise body force f_x in order to avoid non-zero streamwise gradients of mean density and pressure. Hence f_x acts as an "effective pressure gradient" to maintain a prescribed mass flow rate $m = \int_0^{2h} \bar{\rho} \bar{u} dy / 2h$, which is in practice more relevant to explain the physics of a fully developed flow. The mean gradient of the actual, thermal dynamic pressure $d\bar{p}/dx$ is zero [38]. Two types of body force are frequently implemented: volume-based, with $-\left(\frac{\partial p}{\partial x}\right)_{eff} = f_x$, and density-based, with $-\left(\frac{\partial p}{\partial x}\right)_{eff} = \rho f_x$. There is no significant difference regarding the resulting total shear stress profile [47]. In this study, f_x is chosen to be the volume-based one, while Huang *et al.* [47] implemented the second type.

In the temperature transformation, the primary goal is to establish the relationship between the mean temperature gradient and the heat flux. To achieve this, a momentum and energy balance analysis is required.

B. Momentum and energy balance

Consider the control volume from the wall to a reference y -plane, for statistically steady flows, time-derivative and convective terms in wall-parallel directions vanish, leading to the momentum and energy balance, as shown in Fig. 1.

Integrating Eqs. (4) and (5) from the wall to a reference y -plane, we obtain the momentum and

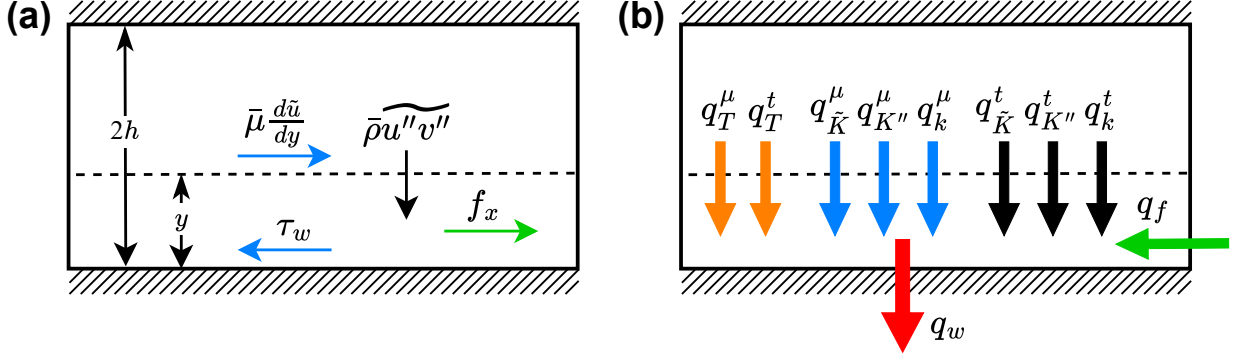


FIG. 1. Momentum (a) and energy (b) balance in a statistically steady turbulent channel flow. h is the channel half-height. The black dashed line indicates a reference y -plane in the lower half-channel ($y/h = 0$ to 1). The expressions for each heat flux component are provided in Eqs. (10) to (20).

energy balance equations:

$$\bar{\mu} \frac{d\tilde{u}}{dy} - \bar{\rho} \tilde{u}'' v'' + \int_0^y f_x(\eta) d\eta = \tau_w. \quad (7)$$

$$\overline{\lambda \frac{dT}{dy}} - \overline{\rho c_p v'' T''} + \overline{\tau_{2i} u_i} - \overline{\rho v'' \frac{1}{2} u_i u_i} + \int_0^y f_x \tilde{u} dy = q_w. \quad (8)$$

Here, $\bar{\mu} d\tilde{u}/dy$ is the mean viscous stress, $-\bar{\rho} \tilde{u}'' v''$ represents the mean turbulent momentum flux, $\int_0^y f_x(\eta) d\eta$ corresponds to the total streamwise body force, and τ_w is the mean wall shear stress. In Eq. (8), q_w is the mean heat flux removed from the wall. The energy fluxes across the y -plane can be categorized into two primary mechanisms: molecular diffusion and turbulent diffusion. Each of these mechanisms involves the diffusion of both thermal energy and kinetic energy.

Before proceeding, we first decompose the instantaneous kinetic energy into three components, analogous to the approach of Huang *et al.* [8, 47] and Chen *et al.* [42]:

$$K = \frac{1}{2} u_i u_i = \frac{1}{2} \tilde{u}_i \tilde{u}_i + \tilde{u}_i u_i'' + \frac{1}{2} u_i'' u_i''. \quad (9)$$

Since the mean flow in spanwise and wall-normal directions is negligible, Eq. (9) simplifies to $K = \tilde{K} + K'' + k$, where $\tilde{K} = \frac{1}{2} \tilde{u}_i \tilde{u}_i \approx \frac{1}{2} \tilde{u} \tilde{u}$, $K'' = \tilde{u}_i u_i'' \approx \tilde{u} u''$, and $k = \frac{1}{2} u_i'' u_i''$.

In Eq. (8), the first two terms represent the molecular and turbulent diffusion of thermal energy (or equivalently molecular and turbulent heat conduction).

$$q_T^\mu = \overline{\lambda \frac{dT}{dy}} \approx \bar{\lambda} \frac{d\tilde{T}}{dy}, \quad (10)$$

$$q_T^t = -\overline{\rho c_p v'' T''}. \quad (11)$$

The third term in Eq. (8) represents the molecular diffusion of kinetic energy, which can be split into three parts:

$$\overline{\tau_{2i}u_i} = \mu \overline{\frac{dK}{dy}} = q_{\tilde{K}}^{\mu} + q_{K''}^{\mu} + q_k^{\mu} \quad (12)$$

with

$$q_{\tilde{K}}^{\mu} = \mu \overline{\frac{d\tilde{K}}{dy}} \approx \bar{\mu} \overline{\frac{d\tilde{u}}{dy}} \tilde{u}, \quad (13)$$

$$q_{K''}^{\mu} = \mu \overline{\frac{dK''}{dy}} = \mu' \overline{\frac{d(\tilde{u}u'')}{dy}}, \quad (14)$$

$$q_k^{\mu} = \mu \overline{\frac{dk}{dy}} \approx \bar{\mu} \overline{\frac{d(u''_i u''_i / 2)}{dy}}. \quad (15)$$

The fourth term in Eq. (8) represents the turbulent diffusion of kinetic energy, which is also split into three parts:

$$-\overline{\rho v \frac{1}{2} u_i u_i} = q_{\tilde{K}}^t + q_{K''}^t + q_k^t \quad (16)$$

with

$$q_{\tilde{K}}^t = -\overline{\rho v'' \tilde{K}} \approx 0, \quad (17)$$

$$q_{K''}^t = -\overline{\rho v'' K''} \approx -\overline{\rho v'' u''} \tilde{u}, \quad (18)$$

$$q_k^t = -\overline{\rho v'' k} = -\overline{\rho v'' \frac{1}{2} u''_i u''_i}. \quad (19)$$

The last term on the left hand side of Eq. (8) is associated with the work of the body force. Considering the overall balance between the body force and wall shear stress in the channel, and assuming a uniform body force per unit volume, we have $f_x = \tau_w/h$. Hence,

$$q_f = \int_0^y f_x \tilde{u}(\eta) d\eta = \tau_w \tilde{u}_b^i \frac{y}{h}, \quad (20)$$

$$\tilde{u}_b^i = \frac{1}{y} \int_0^y \tilde{u}(\eta) d\eta, \quad y \in (0, h]. \quad (21)$$

Here, we introduce the integral bulk velocity, \tilde{u}_b^i , which is connected to the mean velocity profile. Note that the expression of \tilde{u}_b^i should be modified correspondingly if the body force implemented in the solver is density-based, as is the case in Sec. III A.

On the right hand side of Eq. (8), q_w represents the heat flux removed from the channel. Invoking f_x in Eq. (7) and substituting Eqs. (10) to (20) into Eq. (8), we obtain the following momentum and energy balance equation:

$$\bar{\mu} \frac{d\tilde{u}}{dy} - \bar{\rho} \widetilde{u'' v''} = \tau_w \left(1 - \frac{y}{h} \right), \quad (22)$$

$$\underbrace{\bar{\lambda} \frac{d\tilde{T}}{dy}}_{q_T^\mu} - \underbrace{\bar{\rho} c_p v'' T''}_{q_T^t} + \underbrace{\bar{\mu} \frac{d\tilde{u}}{dy} \tilde{u}}_{q_{\tilde{K}}^\mu} + \underbrace{\mu' \frac{d(\tilde{u}u'')}{dy}}_{q_{K''}^\mu} + \underbrace{\bar{\mu} \frac{d(u''_i u''_i/2)}{dy}}_{q_k^\mu} - \underbrace{\bar{\rho} v'' u''}_{q_{K''}^t} \tilde{u} - \underbrace{\bar{\rho} v'' \frac{1}{2} u''_i u''_i}_{q_k^t} + \underbrace{\tau_w \tilde{u}_b^i \frac{y}{h}}_{q_f} = q_w. \quad (23)$$

C. Temperature transformation

Regarding the transformation to account for compressibility, two approaches have been commonly applied in previous studies: wall scaling [18] and semi-local scaling [21, 22, 47], typically referred to as VD-type and SL-type transformations, respectively. The VD-type transformation is motivated by overlap layer balance and neglects viscous effects, while the SL-type transformation considers both viscous and turbulent effects. In this study, we demonstrate that both VD-type and SL-type temperature transformations can in fact be derived directly from the overlap layer, with an additional constraint on the mixing length to ensure consistency in the viscous sublayer.

In the study of Huang *et al.* [8], $q_{K''}^\mu$ is not considered. Both q_k^μ and q_k^t are neglected in the energy balance equations because their magnitudes are significantly smaller than $q_{\tilde{K}}^\mu$ and $q_{K''}^t$, respectively. Chen *et al.* [42] and Cheng and Fu [35] reported similar treatment in the near wall region. However, since we focus on the relationship between $d\tilde{T}/dy$ and q_T^t in the overlap layer, the latter should be the basis for comparison when determining which terms in Eq. (23) can be neglected.

In Fig. 2, the magnitudes of each term in Eq. (23), normalized by q_w and q_T^t , are plotted for three types of wall-boundary conditions in compressible turbulent channel flow: (1) the classical setup with both walls isothermal, (2) the isothermal wall side in mixed isothermal/adiabatic configuration, and (3) the adiabatic wall side in the same mixed configuration. As $q_w = 0$ for adiabatic wall, the heat flux in panel (c) is normalized using q_w at the corresponding isothermal wall side.

Outside the viscous sublayer and buffer layer, the flux components q_T^μ , $q_{\tilde{K}}^\mu$, $q_{K''}^\mu$, q_k^μ and q_k^t are significantly smaller than q_w across all three types of thermal wall-boundary configurations. However, when compared to q_T^t , both $q_{\tilde{K}}^\mu$ and q_k^t exhibit comparable magnitudes in this region for the classical isothermal configuration, as seen in panel (d). Therefore, $q_{\tilde{K}}^\mu$ and q_k^t should be retained in this case.

In contrast, under the mixed thermal configuration, q_T^t is consistently directed from the adiabatic wall toward the cold wall, in agreement with the findings of Zhu *et al.* [48]. Its magnitude remains dominant throughout the outer layer, as shown in panels (e) and (f). Consequently, the

$q_T^\mu = \bar{\lambda} \frac{d\bar{T}}{dy}$	$q_{\tilde{K}}^\mu = \bar{\mu} \frac{d\tilde{u}}{dy} \tilde{u}$	$q_{K''}^\mu = \overline{\mu' \frac{d(\tilde{u}u'')}{dy}}$	$q_k^\mu = \bar{\mu} \frac{d(u''_i u''_i/2)}{dy}$
$q_T^t = -\overline{\rho c_p v'' T''}$	q_f	$q_{K''}^t = -\overline{\rho v'' u''} \tilde{u}$	$q_k^t = -\overline{\rho v'' \frac{1}{2} u''_i u''_i}$

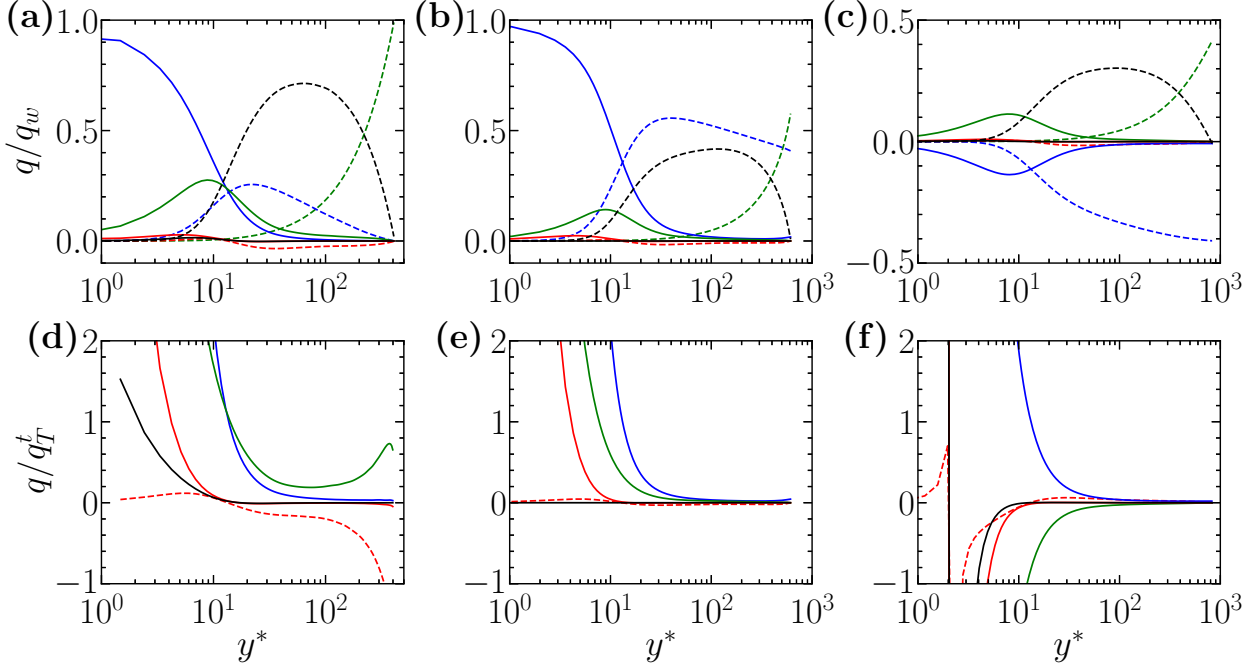


FIG. 2. Energy budget in compressible turbulent channel flow. (a, d): isothermal wall with $M_b = 1.7, Re_b = 10000$ in classical isothermal setup (see table II); (b, e): isothermal wall side with $M_b = 1.86, Re_b = 20813$ in mixed isothermal/adiabatic configuration (case "iF2" in table III); (c, f): adiabatic wall side with $M_b = 1.86, Re_b = 45788$ in mixed isothermal/adiabatic configuration (case "aF2" in table IV). Here, M_b and Re_b represent the bulk Mach number and bulk Reynolds number, respectively, as defined in §III. The heat flux in panel (c) is normalized using q_w from the corresponding isothermal wall side. Negative values indicate heat flux away from the wall (see Fig. 1).

smaller flux components— $q_T^\mu, q_{K''}^\mu, q_k^\mu$, and q_k^t —can be reasonably neglected. In principle, $q_{\tilde{K}}^\mu$ may also be neglected when compared to q_T^t . However, this term can be further simplified in combination with Eq. (22), which improves the overall accuracy. For this reason, Huang *et al.* [8] retained it in the energy balance equation, and we follow the same approach in this work.

Based on above observations, we retain $q_{\tilde{K}}^\mu$ and q_k^t for all three types of thermal wall-boundary conditions, leading to the following simplified energy balance equation:

$$-\overline{\rho c_p v'' T''} = q_w - \tau_{tot} \tilde{u} + \overline{\rho v'' \frac{1}{2} u''_i u''_i} - \tau_w \tilde{u}_b^i \frac{y}{h}. \quad (24)$$

Here, $\tau_{tot} = \bar{\mu} d\tilde{u}/dy - \overline{\rho v'' u''}$ represents the total shear stress. Invoking Prandtl's mixing length hypothesis, $v_t = l_m^2 d\tilde{u}/dy$, along with the turbulent Prandtl number Pr_t , we obtain:

$$-\overline{\rho c_p v'' T''} = \frac{\bar{\rho} v_t c_p}{Pr_t} \frac{d\tilde{T}}{dy}. \quad (25)$$

In the overlap layer, the viscous stress can be neglected. In other words, the total shear stress is approximately equal to the Reynolds stress. Using Boussinesq's assumption, we have:

$$l_m \frac{d\tilde{u}}{dy} = \sqrt{\frac{\tau_{tot}}{\bar{\rho}}}. \quad (26)$$

Note that the general form of l_m is applied in Eqs. (25) and (26). The influence of mixing length model will be presented in subsequent sections. Following Huang *et al.* [8], we define the friction Mach number as $M_\tau = u_\tau / \sqrt{\gamma R \tilde{T}_w}$, the non-dimensional heat flux as $B_q = -q_w / (\bar{\rho}_w c_p u_\tau \tilde{T}_w)$, and the non-dimensional temperature difference as $\theta^+ = (\tilde{T}_w - \tilde{T}) / \tilde{T}_w$. Substituting these definitions and Eqs. (22), (25), (26) into Eq. (24) yields:

$$\frac{l_m \sqrt{\tau_{tot}^+}}{Pr_t} \sqrt{\frac{\bar{\rho}}{\bar{\rho}_w}} \frac{d\theta^+}{dy} = B_q + \left(\tau_{tot}^+ + \frac{\tilde{u}_b^i y}{\tilde{u} h} \right) (\gamma - 1) M_\tau^2 u^+ - \frac{\overline{\rho v'' u''_i u''_i / 2}}{\bar{\rho}_w c_p u_\tau \tilde{T}_w}, \quad (27)$$

Here, $u^+ = \tilde{u}/u_\tau$ and $\tau_{tot}^+ = \tau_{tot}/\tau_w$. For turbulent channel flow driving by volume-based body force, $\tau_{tot}^+ = 1 - y/h$. Furthermore, we define the following three parameters:

$$\psi_1 = \frac{l_m \sqrt{\tau_{tot}^+}}{\kappa y}, \quad \psi_2 = \tau_{tot}^+ + \frac{\tilde{u}_b^i y}{\tilde{u} h}, \quad \psi_3 = \frac{-\overline{\rho v'' u''_i u''_i / 2}}{\bar{\rho}_w c_p u_\tau \tilde{T}_w} \quad (28)$$

Substituting these definitions, we obtain a simplified equation:

$$\frac{\psi_1}{B_q + \psi_2 (\gamma - 1) M_\tau^2 u^+ + \psi_3} \sqrt{\rho^+} d\theta^+ = \frac{Pr_t}{\kappa} \frac{dy}{y}. \quad (29)$$

Here, $\rho^+ = \bar{\rho}/\bar{\rho}_w$. Based on Eq. (29), the VD-type and SL-type transformations can be established by applying wall scaling and semi-local scaling, respectively.

- **VD-type temperature transformation**

Scaling the y -coordinate in Eq. (29) with wall quantities, we obtain:

$$\frac{\psi_1}{B_q + \psi_2 (\gamma - 1) M_\tau^2 u^+ + \psi_3} \sqrt{\rho^+} d\theta^+ = \frac{Pr_t}{\kappa} \frac{dy^+}{y^+}. \quad (30)$$

Here, $y^+ = \sqrt{\tau_w \bar{\rho}_w} y / \bar{\mu}_w$. Following the VD-type transformation [18, 40], and as also done in the derivation of Chen *et al.* [42] and Huang *et al.* [8], we define the VD-type temperature transformation as:

$$T_{VD}^+ = \int_0^{\theta^+} \frac{\psi_1}{B_q + \psi_2 (\gamma - 1) M_\tau^2 u^+ + \psi_3} \sqrt{\rho^+} d\theta^+. \quad (31)$$

According to Eq. (30), T_{VD}^+ is expected to exhibit a logarithmic profile in the overlap layer:

$$T_{VD}^+ = \frac{Pr_t}{\kappa} \log(y^+) + B_{T,VD}. \quad (32)$$

Here, $B_{T,VD}$ is an integration constant, which is usually a function of Prandtl number.

- **SL-type temperature transformation**

Scaling the y -coordinate in Eq. (29) with local quantities, we obtain:

$$\frac{\psi_1}{B_q + \psi_2(\gamma-1)M_\tau^2 u^+ + \psi_3} \sqrt{\rho^+} \left(1 + \frac{1}{2} \frac{y^+}{\rho^+} \frac{d\rho^+}{dy^+} - \frac{y^+}{\mu^+} \frac{d\mu^+}{dy^+} \right) d\theta^+ = \frac{Pr_t}{\kappa} \frac{dy^*}{y^*}. \quad (33)$$

Here $\mu^+ = \bar{\mu}/\bar{\mu}_w$, $y^* = \sqrt{\tau_w \bar{\rho}} y / \bar{\mu}$. The SL-type temperature transformation is defined as:

$$T_{SL}^+ = \int_0^{\theta^+} \frac{\psi_1}{B_q + \psi_2(\gamma-1)M_\tau^2 u^+ + \psi_3} \sqrt{\rho^+} \left(1 + \frac{1}{2} \frac{y^+}{\rho^+} \frac{d\rho^+}{dy^+} - \frac{y^+}{\mu^+} \frac{d\mu^+}{dy^+} \right) d\theta^+. \quad (34)$$

According to Eq. (33), T_{SL}^+ is expected to exhibit a logarithmic profile in the overlap layer:

$$T_{SL}^+ = \frac{Pr_t}{\kappa} \log(y^*) + B_{T,SL}. \quad (35)$$

Here, $B_{T,SL}$ is an integration constant, which may be a function of Prandtl number.

It is important to note that above derivation is entirely based on the logarithmic region, where the viscous shear stress and heat flux are neglected. Therefore, the energy balance relations in Eqs. (30) and (33) are only valid in the logarithmic layer. However, both T_{VD}^+ and T_{SL}^+ defined in Eqs. (31) and (34) are formulated to include the entire half-channel height. This may cause potential physical consistency below the overlap layer, which will be discussed in next section.

- **Distribution in the viscous sublayer**

As the law of the wall includes both the linear law for the viscous sublayer and the log-law for the overlap layer [39, 42, 49]. To satisfy the linear law in the viscous sublayer, additional constraints should be imposed. Before proceeding, we emphasize that T_{VD}^+ and T_{SL}^+ are not redefined in the viscous sublayer. Rather, their distributions defined in Eqs. (31) and (34) are evaluated in this region.

Considering the global energy balance equation, Eq. (23), it can be verified that the molecular heat conduction q_T^μ dominates in the viscous sublayer, while q_k^t and q_f are negligible. Consequently, Eq. (23) reduces to:

$$\frac{\bar{\mu} c_p}{Pr} \frac{d\tilde{T}}{dy} = q_w - \tau_{tot} \tilde{u}. \quad (36)$$

The right hand side of Eq. (24) is approximately equal to the right hand side of Eq. (36). In this case, the denominator in Eqs. (31) and (34) reduces to:

$$B_q + \psi_2(\gamma - 1)M_\tau^2 u^+ + \psi_3 \approx \frac{\bar{\mu}}{Pr\bar{\rho}_w u_\tau} \frac{d\theta^+}{dy}. \quad (37)$$

Invoking Eq. (37) to Eqs. (31) and (34), and applying corresponding scaling, we obtain:

$$T_{VD}^+ \approx Pr \int_0^{y^+} \psi_1 \frac{\sqrt{\rho^+}}{\mu^+} dy^+, \quad T_{SL}^+ \approx Pr \int_0^{y^*} \psi_1 dy^*. \quad (38)$$

As stated earlier, Eq. (38) does not redefine the transformations in the viscous sublayer. Rather, it represents the equivalent distributions of the proposed transformations, Eqs. (31) and (34), in this region. Furthermore, it also accounts for the different near-wall behaviors of the two transformations over isothermal and adiabatic walls (see Sec. III).

In order to follow the linear law [42, 49] in the viscous sublayer ($0 \leq y^+ \leq 5$), the proposed transformations should meet additional requirements such that:

$$T_{VD}^+ \approx Pr y^+, \quad T_{SL}^+ \approx Pr y^*. \quad (39)$$

For the SL-type transformation, Eqs. (38) and (39) imply:

$$\psi_1 = \frac{l_m \sqrt{\tau_{tot}^+}}{\kappa y} \approx 1, \quad (40)$$

which indicates

$$l_m \approx \frac{\kappa y}{\sqrt{\tau_{tot}^+}}. \quad (41)$$

Typically, $\tau_{tot}^+ \approx 1$ in this region for turbulent channel, pipe, and zero pressure gradient boundary layer flows. Hence, the requirement of $\psi_1 \approx 1$ is equivalent to $l_m \approx \kappa y$ in the viscous sublayer.

For the VD-type transformation, this requirement still holds. However, due to the presence of ρ^+ and μ^+ in Eq. (38), the performance of the VD-type temperature transformation is generally not as good as the SL-type in the viscous sublayer and buffer layer.

It should be noted that, the eddy viscosity is typically damped in the viscous sublayer, as shown in previous transformations [8, 50] and near-wall modeling [51, 52]. The damped eddy viscosity corresponds to a damped l_m . According to She *et al.* [53], l_m has multi-layer structure, with $l_m \sim y^{3/2}$ in the viscous sublayer, $l_m \sim y^2$ in the buffer layer, and $l_m \sim y$ in the logarithmic layer. However, Eq. (41) implies that wall damping should not be employed in our transformation. These observations may lead to conceptual inconsistency in the mixing length l_m , which is a limitation of the present transformation. In this regard, we make the following comments.

First, $l_m d\tilde{u}/dy$ in Eq. (26) is directly related to the total shear stress τ_{tot}^+ in the overlap layer, and τ_{tot}^+ is subsequently incorporated into the energy balance equation and the parameter ψ_1 . When the transformations are defined to include the viscous sublayer, adopting the relation $l_m \approx \kappa y$ effectively removes the explicit influence of l_m in ψ_1 . As a result, only the total shear stress τ_{tot}^+ is retained. In other words, $l_m \approx \kappa y$ implicitly preserves the viscous effects in the sublayer. The parameter ψ_1 serves as a modulating factor that explicitly accounts for the turbulent diffusion in the overlap layer and implicitly approximates the viscous effects within the viscous sublayer.

Second, for the velocity transformation, a fundamental requirement is that $dU_I^+/dY_I^+ = \tau_y/\tau_w \approx 1$ in the viscous sublayer. Here, Y_I^+ and U_I^+ denote the transformed "incompressible" coordinate and velocity [23, 33], respectively, and τ_y is the local shear stress. Analogously, for the temperature transformation, the corresponding requirement within the viscous sublayer is $dT_I^+/dY_I^+ = Pr q_y/q_w \approx Pr$, where T_I^+ is the transformed "incompressible" temperature and q_y is the local heat flux. According to Eq. (38), the transformed temperature gradient in the viscous sublayer is given by $dT_{SL}^+/dy^* = Pr \psi_1$. The undamped $l_m \approx \kappa y$ ensures $\psi_1 \approx 1$, and hence $dT_{SL}^+/dy^* \approx Pr$.

Finally, one may also follow the approach as done by Hasan *et al.* [50], Modesti and Pirozzoli [43], and Huang *et al.* [8] to derive the semi-local type transformation, in which both molecular and turbulent diffusions can be incorporated. Nevertheless, in the final transformation of Huang *et al.* [8], the molecular and turbulent Prandtl number are not included in the final expression. In this case, the transformation proposed by Huang (2023) can be regarded as a special form of Eq. (34) by setting $\psi_1 = 1$, $\psi_2 = 1$, and $\psi_3 = 0$. The introduction of ψ_1 , ψ_2 , and ψ_3 offers the potential for developing more advanced transformations in the future.

- **Mixing length model**

The above analysis indicate that the desired mixing length model in our transformations should satisfy the following two requirements: (1) it follows $l_m \approx \kappa y$ in the viscous sublayer, and (2) it is capable of modeling the Reynolds stress $\bar{\rho} \widetilde{u''v''}$ in the overlap layer. Both T_{VD}^+ and T_{SL}^+ given in Eqs. (31) and (34) naturally transition from the log-law in the overlap layer to the linear law in the viscous sublayer. Various mixing length models have been developed in the literature. In principle, any suitable model can be applied. In the following, we introduce three representative models that can be applied to illustrate different characteristics of the transformation.

The first model is the most widely utilized linear formulation based on Prandtl's hypothesis of

linear variation of mixing length:

$$l_m^L = \kappa y. \quad (42)$$

It satisfies the first requirement while is not well-suited for the second. As a result, the transformed temperature follows the linear law in the viscous sublayer, while only exhibiting a logarithmic behavior in the overlap layer at sufficiently high Reynolds numbers.

The second model is a special case for the channel flow configuration [44, 54]. The study by Pirozzoli [44] indicates that the linear variation of total shear stress and the velocity log-law directly yields the parabolic form:

$$l_m^P = \kappa y \sqrt{1 - \frac{y}{h}}. \quad (43)$$

It satisfies both requirements, and hence leads to a linear distribution in the viscous sublayer and a clear logarithmic profile in the overlap layer. Moreover, the transformed temperatures coincides with their incompressible counterparts at comparable characteristic Reynolds number.

The third model is the enhanced mixing length formulation proposed by Xu *et al.* [55], motivated by the idea of extending the logarithmic profile in the outer layer:

$$\frac{l_m^E}{h} = \begin{cases} \kappa \frac{y}{h} \sqrt{1 - \frac{y}{h}} & \text{for } y/h \in [0, \eta_{mix}], \\ \frac{K_{mix}(1 - r^{M_{mix}})}{M_{mix}(1 + r_{core}^2)^{1/4}} \left[1 + \left(\frac{r_{core}}{r} \right)^2 \right]^{1/4} & \text{for } y/h \in (\eta_{mix}, 1], \end{cases} \quad (44)$$

$$\eta_{mix} = 0.060 + 0.340 \exp(-Re_\tau^*/595), \quad (45)$$

$$K_{mix} = 0.416 + 0.172 \exp(-Re_\tau^*/373), \quad (46)$$

$$M_{mix} = 3.104 + 0.871 \exp(-Re_\tau^*/3144). \quad (47)$$

Here, $r = 1 - y/h$, $r_{core} = 0.45$, and $Re_\tau^* = \bar{\rho}_c \sqrt{\tau_w / \bar{\rho}_c} h / \bar{\mu}_c$, which represents the semi-local-scaled friction Reynolds number, with the subscript c denoting quantities at the channel centerline. In the first part, the parabolic form is applied, which aligns Eq. (41) in the viscous sublayer. The second part is a revised form of the model by She *et al.* [53], originally developed for incompressible turbulent channel flow. In our tests, their model performs well at $Re_\tau = 1000$, but its accuracy deteriorates for $Re_\tau < 400$ and $Re_\tau > 4000$, where $Re_\tau = \rho_w u_\tau h / \bar{\mu}_w$ is the friction Reynolds number. Outside this range the performance in the outer layer degrades. Although Zhu *et al.* [56] proposed a revised version by applying semi-local scaling, the l_m distribution in the outer layer does not significantly differ. In this regard, Eq. (44) introduces three parameters, η_{mix} , K_{mix} , and M_{mix} , to more effectively account for Reynolds and Mach number effects in the outer layer.

In addition to meeting the first requirement, the enhanced model l_m^E also satisfies the second over a significantly wider region beyond the overlap layer. In this study, it is used to demonstrate that, with a suitable mixing length model, the transformed temperature would exhibit an extended logarithmic profile.

Moreover, to illustrate the damping effects, we consider the linear model with a Van Driest damping function [53, 57]:

$$l_m^{LD} = \kappa y \left[1 - \exp \left(-y^*/A^+ \right) \right] \text{ with } A^+ = 27 \quad (48)$$

It is used to demonstrate that the mixing length indeed should remain undamped in the proposed transformation. Note that the value of A^+ is different from those used in the eddy viscosity models [52, 58].

Apart from the l_m , we adopt the von Kármán constant $\kappa = 0.41$ following Pope [5], although recent studies have reported slightly different values [9, 11, 53, 59]. For the turbulent Prandtl number, we use $Pr_t = 0.85$, which has been reported by Lusher and Coleman [38] to be appropriate for both isothermal and adiabatic walls in the logarithmic layer. The same value is also reported in Coles [39]. Additionally, Huang *et al.* [8] proposed the relation $Pr_t = 1.05 - 0.2 \tanh^3(-y^*/17)$, which also yields $Pr_t \approx 0.85$ in the logarithmic region.

Regarding the three additional parameters given in Eqs. (31) and (34), ψ_1 can be computed following approaches introduced above, while ψ_2 and ψ_3 can be directly computed from the simulation results. Note that the influence of the body force is incorporated through the ratio \tilde{u}_b^i/\tilde{u} . Representative distributions of \tilde{u}_b^i/\tilde{u} are shown in Fig. 17 in Appendix A.

III. PERFORMANCE OF TEMPERATURE TRANSFORMATION

In this section, we first examine the influence of mixing length model on the transformation, and then evaluate the performance of the temperature transformations using data from direct numerical simulations (DNS) and wall-resolved large eddy simulations (WRLES) of compressible turbulent channel flow. Specifically, we utilize:

- DNS from Gerolymos and Vallet [60, 61, 62] with isothermal wall boundary condition and density-based body force.
- WRLES from our own computations with isothermal wall boundary condition and volume-based body force.

- DNS from Lusher and Coleman [38] with mixed adiabatic/isothermal wall boundary condition and volume-based body force.

Details of these data are provided in table I to table IV. Additionally, we compare the performance of our transformations with those proposed by Chen *et al.* [42], Huang *et al.* [8], and Cheng and Fu [35], as given by Eq. (B1) to (B5) in Appendix B. The DNS result of Pirozzoli *et al.* [15] for the temperature profile in turbulent channel flow at $Re_\tau \approx 4000$ and $Pr = 0.71$ is also included for reference.

Before proceeding, we define the bulk Mach number $M_b = u_b / \sqrt{\gamma R \tilde{T}_w}$ and bulk Reynolds number $Re_b = \rho_b u_b h / \bar{\mu}_w$, where $\rho_b = \int_0^h \bar{\rho} dy / h$, $u_b = \int_0^h \bar{\rho} u dy / (\rho_b h)$. All other terms are as defined in section Sec. II.

A. Performance above the isothermal wall with density-based driving force

In the DNS of Gerolymos and Vallet [60, 61, 62], hereafter referred to as GV2024, the authors investigated the statistics of total and static temperature in compressible turbulent channel flow, along with the effects of Mach number on pressure fluctuations. Both bottom and top walls are isothermal boundary condition. This dataset cover a wide range of Mach and Reynolds numbers, making it well-suited for evaluating the performance of our transformations. Table I lists the critical information of the data. Since the Re_τ^* is relatively low in many of their simulations, only those with $Re_\tau^* > 140$ are considered to mitigate strong low-Reynolds-number effects [33, 58].

It is important to note that the flow in this dataset is driven by density-based body force ρf_x rather than volume-based force f_x [63]. Consequently, the density profile, $\bar{\rho} / \rho_b$, should be considered when calculating ψ_2 . Following Huang *et al.* [47], the total shear stress profile in Eq. (22) and the definition of \tilde{u}_b^i in Eq. (21) should be computed as follows:

$$\bar{\mu} \frac{d\tilde{u}}{dy} - \bar{\rho} \widetilde{u''v''} = \tau_w \left(1 - \frac{1}{h} \int_0^y \frac{\bar{\rho}(\eta)}{\rho_b} d\eta \right), \quad (49)$$

$$\tilde{u}_b^{i,\rho} = \frac{1}{y} \int_0^y \frac{\bar{\rho}}{\rho_b} \tilde{u}(\eta) d\eta. \quad (50)$$

Subsequently, we obtain:

$$\psi_2^\rho = 1 - \frac{1}{h} \int_0^y \frac{\bar{\rho}(\eta)}{\rho_b} d\eta + \frac{\tilde{u}_b^{i,\rho} y}{\tilde{u}}, \quad (51)$$

which is used to calculate T_{VD}^+ and T_{SL}^+ .

TABLE I. DNS of Gerolymos and Vallet [60, 61, 62] for compressible turbulent channel flow with isothermal wall boundary conditions on both the bottom and top walls. The case name in the first column follows the same nomenclature of this database. For instance, "MCLx0p32" refers to Mach number at channel center line, $M_{CLx} = \bar{u}_{CL}/\bar{a}_{CL} = 0.32$, where \bar{u}_{CL} and \bar{a}_{CL} are the mean streamwise velocity and sound speed at the channel center line, respectively.

Case	M_b	Re_b	Re_τ	Re_τ^*	M_τ	$-B_q$
GV2024-MCLx0p32	0.28	2197	145	143	0.0181	0.0020
GV2024-MCLx0p79	0.71	2508	168	151	0.0437	0.0123
GV2024-MCLx0p35	0.30	2786	180	177	0.0191	0.0023
GV2024-MCLx1p99	2.39	6909	555	245	0.1005	0.0963
GV2024-MCLx0p83	0.75	4479	282	251	0.0430	0.0129
GV2024-MCLx1p47	1.49	5468	377	254	0.0757	0.0451
GV2024-MCLx0p80	0.72	6266	378	340	0.0402	0.0117
GV2024-MCLx1p51	1.56	7813	523	342	0.0750	0.0468
GV2024-MCLx1p50	1.57	25216	1479	965	0.0660	0.0414
GV2024-MCLx0p81	0.74	21092	1100	985	0.0356	0.0106

1. Influence of mixing length model

We compare the distribution of l_m and its influence on the transformed temperature, as shown in Fig. 3. Three flow conditions are considered: $M_b = 0.30$ and $Re_\tau^* = 177$; $M_b = 2.39$ and $Re_\tau^* = 245$; $M_b = 1.57$ and $Re_\tau^* = 965$, respectively. These cases represent conditions ranging from weakly to strongly compressible and from weakly to highly turbulent flows.

In the viscous sublayer, only the model with damping function correctly follows the true l_m value. However, the resulting T_{SL}^+ exhibits a lower magnitude due to the damping, as indicated by the red solid lines in panels (g, h, i). On the contrary, the other three models provide the correct linear distributions of T_{SL}^+ , which agree well with the incompressible temperature profile.

In the overlap region, all these models produce logarithmic profile in T_{SL}^+ , although the range varies in different flow conditions. Particularly, for turbulent channel flow, the parabolic model l_m^P gives better performance than the linear model l_m^L in the overlap region, yielding a clearer logarithmic profile. The enhanced model l_m^E produces T_{SL}^+ with an extended logarithmic profile

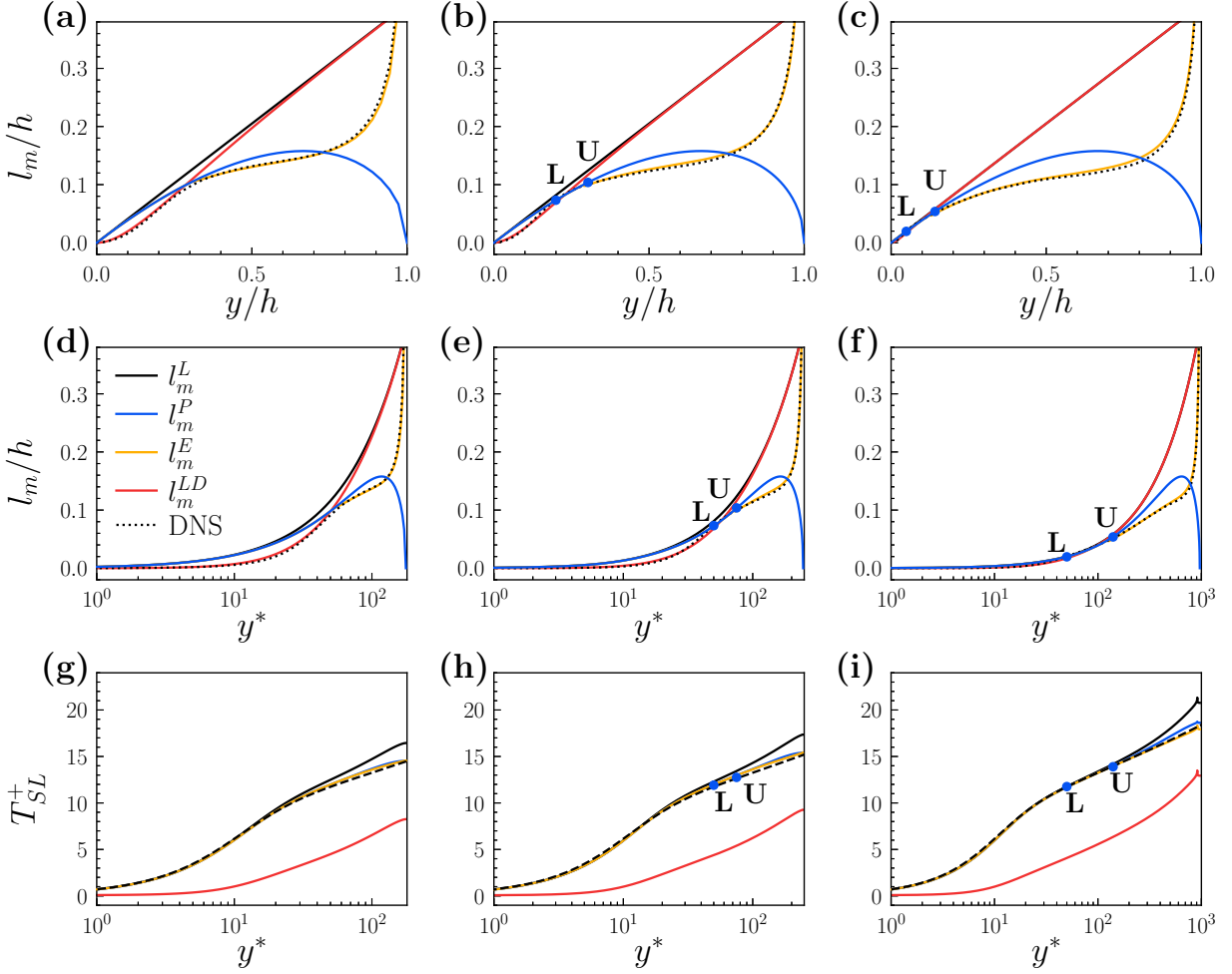


FIG. 3. Distribution of mixing length model and its influence on the transformed temperature. l_m^L , l_m^P , l_m^E , and l_m^{LD} correspond to models given by Eqs. (42), (43), (44), and (48), respectively. Cases included are: $M_b = 0.30$ and $Re_\tau^* = 177$ for (a, d, g), $M_b = 2.39$ and $Re_\tau^* = 245$ for (b, e, h), $M_b = 1.57$ and $Re_\tau^* = 965$ for (c, f, i). DNS data from Gerolymos and Vallet [60, 61, 62] are employed. The black dotted lines represent the theoretical value from DNS using $l_m = (\widetilde{-u''v''})^{1/2}/(d\tilde{u}/dy)$. Points L and U are the approximate lower and upper bound of the logarithmic region using l_m^P . The black dashed lines in (g, h, i) represent the incompressible result of Pirozzoli *et al.* [15] for the temperature profile in turbulent channel flow at $Re_\tau \approx 4000$ and $Pr = 0.71$.

that reaches nearly the channel centerline.

It should be noted that, the damped l_m^{LD} also produces logarithmic profile, but its magnitude is significantly lower. Such underprediction of T_{SL}^+ does not imply that the common practice of applying damping function in the viscous sublayer is incorrect. Rather, it suggests that the l_m

should remain undamped for the present transformation. As introduced in Sec. II C, the present transformation is derived from energy balance in the overlap layer, and the viscous effects are not explicitly included. Consistency in viscous sublayer is achieved by requiring $l_m \approx \kappa y$. This represents a limitation of present transformation. In this regard, one may also follow the approach as done by Hasan *et al.* [50], Modesti and Pirozzoli [43], and Huang *et al.* [8] to explicitly incorporate the viscous and turbulent effects.

Comparing the l_m^P and corresponding T_{SL}^+ profiles between points L and U , it is evident that the approximate overlap region between the model predicted l_m and theoretical values also corresponds to the approximate logarithmic region of T_{SL}^+ . The l_m^E profile aligns with the DNS values in most of the outer layer, and hence provides the broadest range of logarithmic temperature profile. These observations are consistent with the findings of Xu *et al.* [55] regarding the transformed velocity profile in compressible turbulent channel flows.

Above analysis leads to three conclusions: (1) At high Reynolds numbers, applying the commonly used linear model l_m^L in the transformation recovers the temperature law of the wall. (2) Damping effects results in lower magnitude of the transformed temperature. (3) The enhanced model l_m^E provides a better prediction of l_m in the outer layer, resulting in a more pronounced logarithmic region.

In the following, we evaluate the performance of the proposed transformations across various flow conditions using l_m without damping effects.

2. Transformed temperature profile

The temperature profiles under the VD-type and SL-type transformations are shown in Fig. 4 and 5, along with those of Chen *et al.* [42], Huang *et al.* [8] and Cheng and Fu [35] for comparison. Our transformation outperforms the others in both slope and magnitude. As the Reynolds number increases, transformations by Chen *et al.* [42], Huang *et al.* [8] and Cheng and Fu [35] yield improved results, suggesting that the log-law may be achieved at sufficiently high Reynolds numbers. In contrast, our transformations produce a logarithmic profile even at relatively low Reynolds numbers when l_m^P and l_m^E are applied. The linear model l_m^L achieves the log-law only at high Reynolds numbers.

By accounting for density and viscosity variations, the SL-type transformation more effectively collapses the temperature profile in the viscous sublayer and buffer layer than the VD-type, thereby

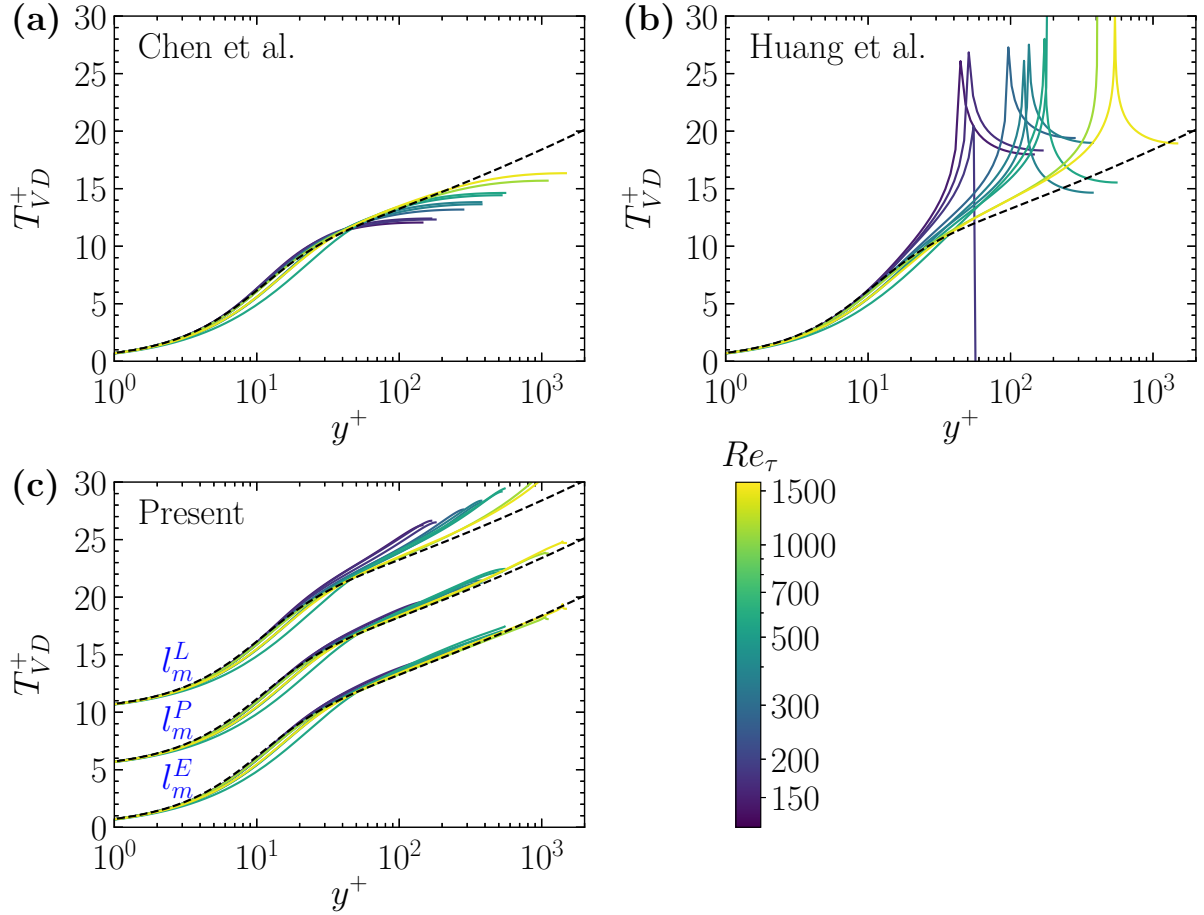


FIG. 4. Temperature profiles above the isothermal wall under the VD-type transformation of (a) Chen *et al.* [42], (b) Huang *et al.* [8], and (c) the present transformation given by Eq. (31), using DNS data from Gerolymos and Vallet [60, 61, 62]. Additional details are provided in table I. All subfigures share the same color bar. In panel (c), results from l_m^P and l_m^L are shifted upward by 5 and 10 units, respectively. Black dashed line: the incompressible DNS result of Pirozzoli *et al.* [15] for the temperature profile in turbulent channel flow at $Re_\tau \approx 4000$ and $Pr = 0.71$.

recovering the law of the wall for temperature. Analogous to velocity transformation, it is expected that the compressible temperature profiles can be mapped onto their incompressible counterparts. In our transformation, T_{SL}^+ profiles using l_m^P show good agreement with the incompressible profile at comparable characteristic Reynolds numbers throughout the entire boundary layer, as demonstrated by the blue dotted line in Fig. 5 (d). The two cases with $M_b = 1.57, Re_\tau^* = 965$ and $M_b = 0.74, Re_\tau^* = 985$ have values of Re_τ^* comparable to the $Re_\tau \approx 1000$ of the incompressible DNS data.

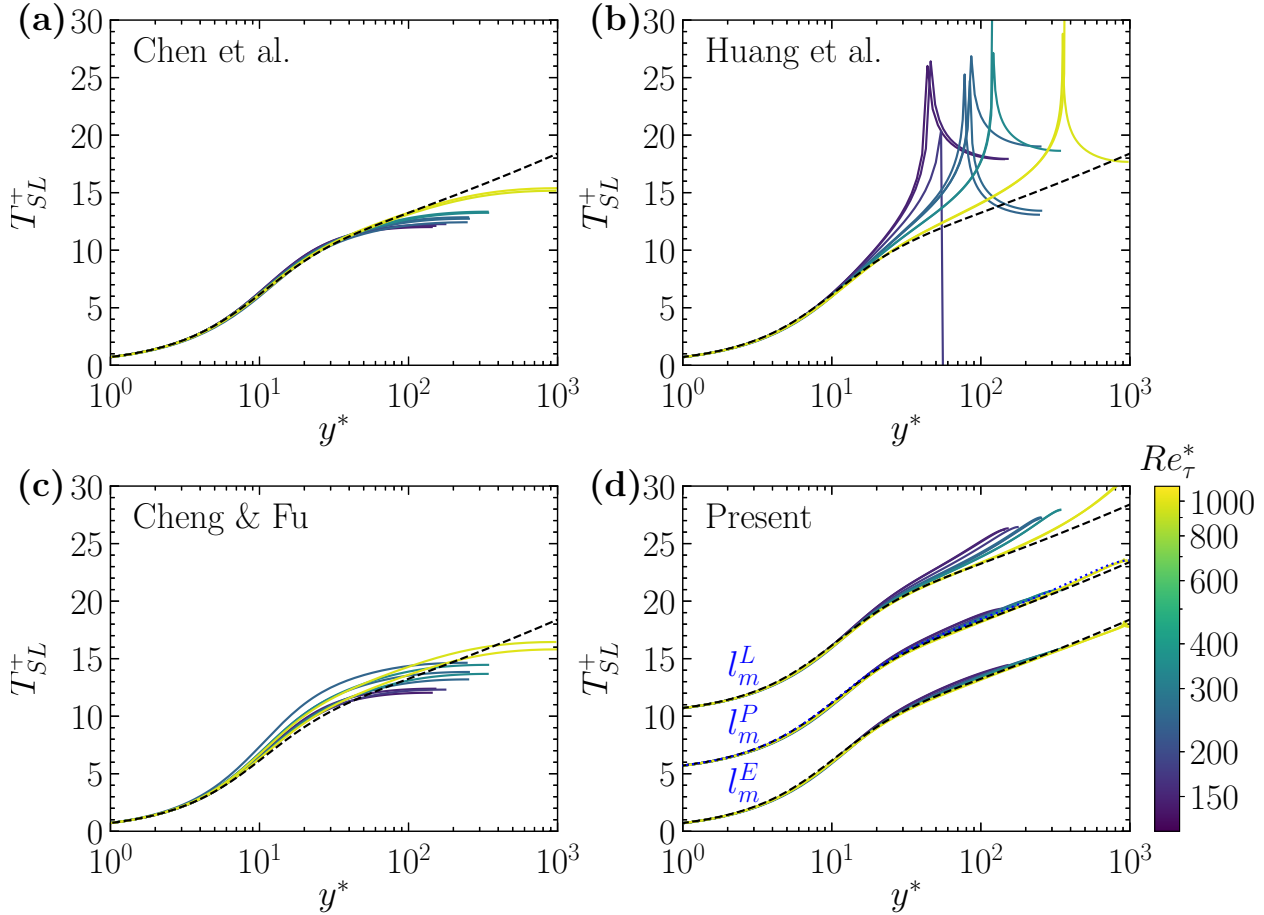


FIG. 5. Temperature profiles above the isothermal wall under the SL-type transformation of (a) Chen *et al.* [42], (b) Huang *et al.* [8], (c) Cheng and Fu [35], and (d) the present transformation given by Eq. (34), using DNS data from Gerolymos and Vallet [60, 61, 62]. Additional details are provided in table I. All subfigures share the same color bar. In panel (d), results from l_m^P and l_m^L are shifted upward by 5 and 10 units, respectively. The black dashed lines are the same as Fig. 4. The blue dotted line corresponds to incompressible case at $Re_\tau \approx 1000$ from Pirozzoli *et al.* [15].

In addition, the SL-type transformation using l_m^E collapses the entire outer layer, producing an extended logarithmic profile. These results for temperature transformation are consistent with the extended logarithmic behavior observed for velocity transformation [55], suggesting a similarity between velocity and temperature statistics. For the T_{SL}^+ using l_m^E in Fig. 5 (d), the black dashed line exhibits slightly higher values for approximately $y^+ > 300$. This is expected, as the incompressible temperature profile at $Re_\tau^+ \approx 4000$ gradually departs the logarithmic profile beyond this range. Similar behavior is also observed in the subsequent sections.

To quantitatively evaluate the logarithmic profile, we compute the log-law intercept B_T . Following the approach of Trettel and Larsson [21], B_T can be determined by computing the integral average of the profile within the logarithmic region.

$$B_T = \frac{1}{y_u^+ - y_l^+} \int_{y_l^+}^{y_u^+} \left(T^+ - \frac{Pr_t}{\kappa} \log(y^+) \right) dy^+ \quad (52)$$

where T^+ denotes the transformed temperature, which may correspond to either T_{VD}^+ or T_{SL}^+ , and y_l^+ and y_u^+ represent the lower and upper bounds of the logarithmic layer, respectively. This region is typically located within the range $y^+ > 30$ and $y/h < 0.3$ [5]. For compressible turbulent flows, two modifications are applied. First, the buffer layer is observed to be thicker than in incompressible flows, leading to an outward shift of the logarithmic layer [21, 50]. Second, y^* is employed for the SL-type transformation, as previously adopted in Guo *et al.* [49]. Accordingly, we set $y_l^+ = 50, y_u^+ = y^+|_{y=0.3h}$ for the VD-type transformation and $y_l^* = 40, y_u^* = y^*|_{y=0.3h}$ for the SL-type transformation.

In our transformation, B_T exhibits a decreasing trend with increasing Re_τ^* under the SL-type transformation, resembling the behavior of velocity transformations [40]. In addition, B_T is also influenced by the strength of wall cooling. Considering the last two cases in table I, we obtain $B_T \approx 3.65$ for $M_b = 1.57, Re_\tau^* = 965$ and $B_T \approx 3.68$ for $M_b = 0.74, Re_\tau^* = 985$, aligning with the $B_T \approx 3.0$ to 4.0 range reported by Brun *et al.* [20]. The value of B_T is slightly larger under the VD-type transformation. Based on the DNS data of Pirozzoli *et al.* [15], the intercept of the incompressible temperature profile at $Re_\tau \approx 4000$ is approximately 3.73 when using $y_l^+ = 50$ and $y_u^+ = 300$, which is close to our results. Slight differences may occur when different values of y_l^+ , y_u^+ , κ , and Pr_t are employed.

In addition, a distinct spike occurs in the transformation by Huang *et al.* [8], which is attributed to the energy imbalance. A more detailed discussion about this issue will be presented in Sec. IV. A similar, but smaller, spike is also observed in our transformations, likely due to the implementation of density-based body force, as no such spikes are observed in our WRLES with volume-based body force (see Sec. III B). Given this, it can be neglected here.

B. Performance above the isothermal wall with volume-based driving force

Unlike the dataset GV2024, which employs a density-based body force and a flow-dependent Prandtl number (Pr), we conduct WRLES of turbulent channel flow driven by a uniform volume-

TABLE II. WRLES with JAX-Fluids [64, 65] for compressible turbulent channel flow with isothermal wall boundary conditions. "JXF-M1.5Re3000" refers to a case at $M_b = 1.5, Re_b = 3000$. The other cases follow the same nomenclature. $\Delta x^+, \Delta y_w^+, \Delta y_c^+, \Delta z^+$ are the mesh sizes in wall units, with subscript w and c representing mesh adjacent to the wall and at the channel center.

Case	M_b	Re_b	Re_τ	Re_τ^*	M_τ	$-B_q$	Δx^+	Δy_w^+	Δy_c^+	Δz^+
JXF-M0.7Re11750	0.7	11750	645	586	0.0356	0.0100	15.84	1.01	13.95	10.56
JXF-M0.8Re3000	0.8	3000	198	175	0.0478	0.0153	11.67	0.63	8.56	8.64
JXF-M0.8Re7667	0.8	7667	450	397	0.0425	0.0136	17.45	0.97	13.33	10.09
JXF-M1.5Re3000	1.5	3000	218	145	0.0797	0.0486	12.85	0.69	9.42	9.52
JXF-M1.5Re7667	1.5	7667	505	341	0.0721	0.0435	16.53	0.95	13.10	9.92
JXF-M1.5Re17000	1.5	17000	1023	696	0.0661	0.0397	20.08	0.74	26.98	14.34
JXF-M1.7Re10000	1.7	10000	664	412	0.0768	0.0526	16.29	1.03	14.34	10.86

based body force and fixed Pr , aligning with the derivation in Sec. II. These simulations were performed using JAX-Fluids [64, 65]. The solver has been verified by prior studies [64–66].

The working fluid is assumed to be ideal gas with constant ratio of specific heats $\gamma = 1.4$ and $Pr = 0.7$. The dynamic viscosity follows a power law relationship with temperature, given by $\mu/\mu_w = (T/T_w)^{0.7}$. A uniform grid is employed in streamwise and spanwise direction, while a stretched grid, following a tangent-hyperbolic function, is used in the wall-normal direction to improve the near wall resolution. We perform implicit large eddy simulation(ILES) in JAX-Fluids, utilizing the Adaptive Local Deconvolution Method (ALDM) developed by Adams *et al.* [67], Hickel and Adams [68], and Hickel *et al.* [69]. Fourth order central finite-difference is used to compute the dissipative fluxes, while third-order Runge-Kutta (RK3) is employed for time integration. No-slip, isothermal boundary conditions are imposed on the bottom and top walls, with periodic boundary conditions applied in the streamwise and spanwise directions. A summary of the simulation is provided in table II.

Fig. 6 and 7 present the transformed temperature profiles for the VD-type and SL-type, respectively, along with those of Chen *et al.* [42], Huang *et al.* [8] and Cheng and Fu [35] for comparison. Although with different driving force, the results closely resemble those of GV2024, with the SL-type transformation providing a better collapse than the VD-type in the viscous sublayer and buffer layer. Our transformations outperform those of Chen *et al.* [42], Huang *et al.* [8], and Cheng and

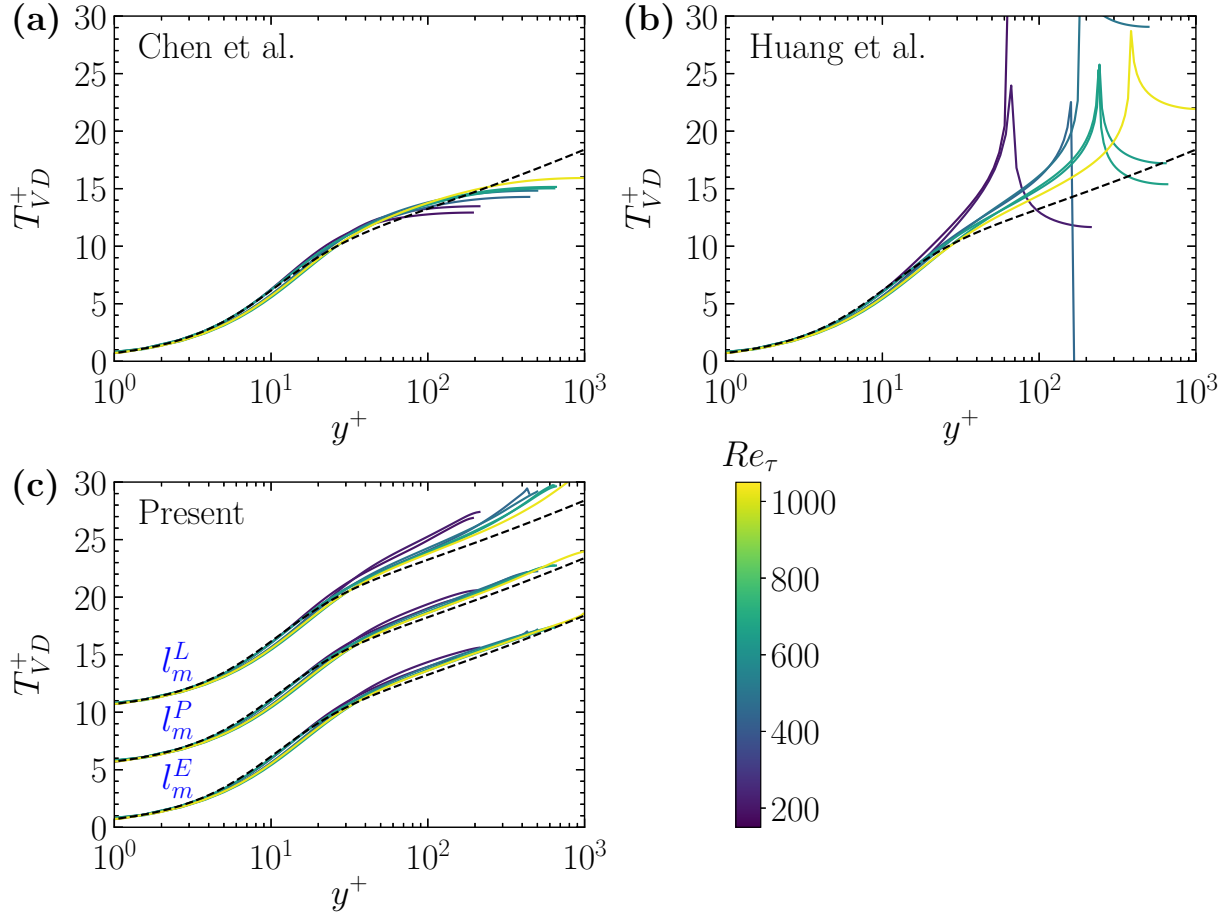


FIG. 6. Temperature profiles above the isothermal wall under the VD-type transformation of (a) Chen *et al.* [42], (b) Huang *et al.* [8], and (c) the present transformation given by Eq. (31), using WRLES dataset. Additional details are provided in table II. All subfigures share the same color bar. In panel (c), results from l_m^P and l_m^L are shifted upward by 5 and 10 units, respectively. The black dashed lines are the same as Fig. 4.

Fu [35], regardless of the applied mixing length model. Additionally, as shown by the blue dotted line in Fig. 7 (d), the T_{SL}^+ using l_m^P at $M_b = 0.7, Re\tau = 586$ agrees well with the incompressible temperature profile at $Re\tau \approx 550$.

C. Performance above the isothermal wall with mixed thermal boundary condition

In this section, we evaluate the performance of our transformations on the isothermal wall side under mixed isothermal/adiabatic boundary conditions. We use the DNS data from Lusher and Coleman [38], hereafter referred to as LC2022. They conducted DNS to study the behavior of

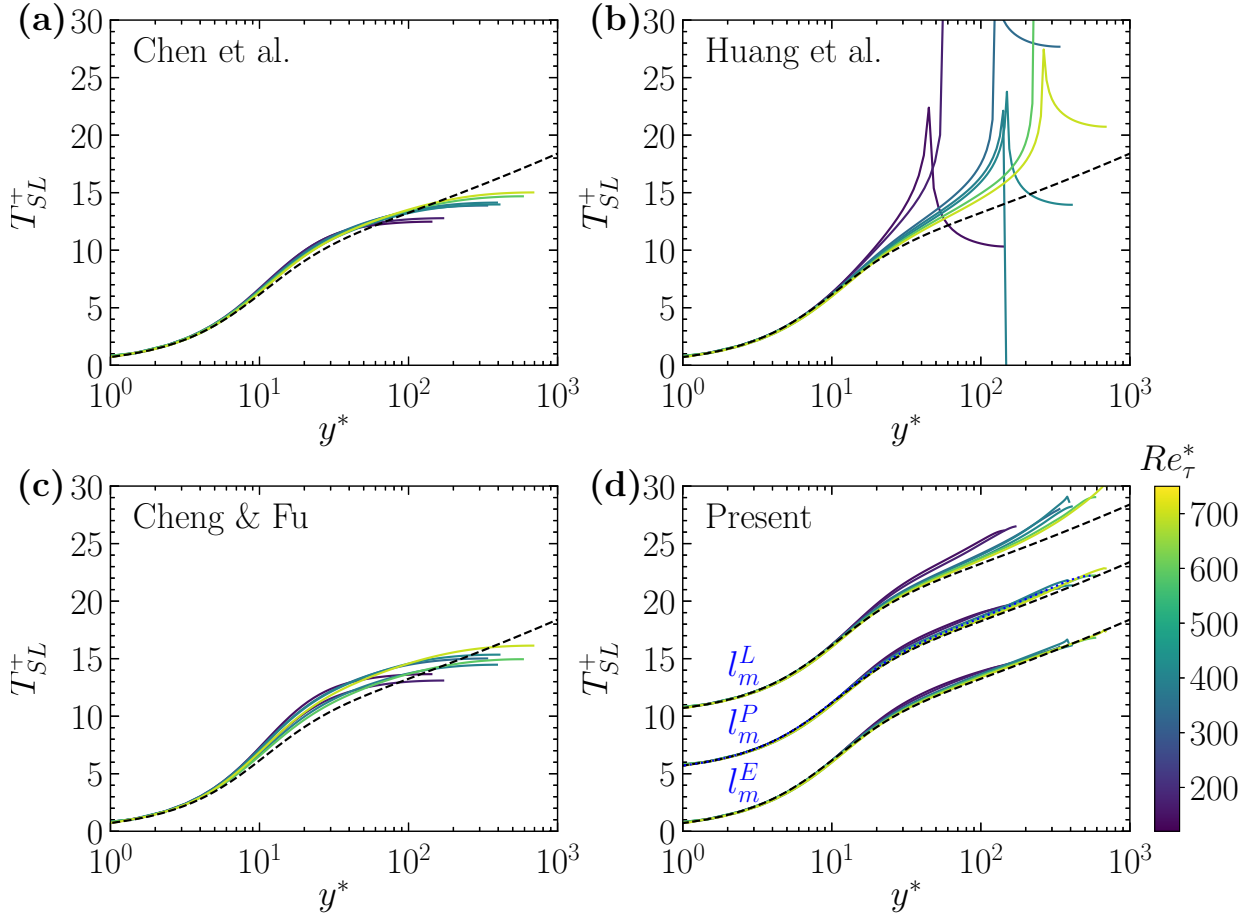


FIG. 7. Temperature profiles above the isothermal wall under the SL-type transformation of (a) Chen *et al.* [42], (b) Huang *et al.* [8], (c) Cheng and Fu [35], and (d) the present transformation given by Eq. (31), using WRLES dataset. Additional details are provided in table II. All subfigures share the same color bar. In panel (d), results from l_m^P and l_m^L are shifted upward by 5 and 10 units, respectively. The black dashed lines are the same as Fig. 4. The blue dotted line corresponds to incompressible case at $Re_\tau \approx 550$ from Pirozzoli *et al.* [15].

turbulent Prandtl number in compressible turbulent channel flows, with no-slip isothermal condition on the bottom wall and adiabatic condition on the top. This setup creates an asymmetric flow field, where the maximum mean velocity shifted from the channel center toward the adiabatic wall, and the temperature increasing from the isothermal side to the adiabatic wall side. Such a setup is well suited for evaluating the transformations in asymmetric flows. Critical data for the isothermal and adiabatic walls are provided in table III and IV, respectively.

Note that the boundary layer thickness is defined as the distance from the maximum velocity

TABLE III. Flow quantities on the isothermal wall side of compressible turbulent channel flows under the mixed thermal configuration. The values are compatible with that of Lusher and Coleman [38] and Huang *et al.* [8].

Case	M_b	Re_b	Re_τ	Re_τ^*	M_τ	$-B_q$	\bar{T}_w/\bar{T}_e
LC2022-iC	2.25	9983	1358	251	0.0723	0.1187	0.244
LC2022-iD	1.70	13846	1436	426	0.0614	0.0767	0.363
LC2022-iD2	1.78	14512	1553	453	0.0630	0.0782	0.358
LC2022-iE	3.44	20638	3789	306	0.0757	0.1886	0.122
LC2022-iE2s	3.96	23770	3260	496	0.0994	0.1701	0.215
LC2022-iF2	1.86	20813	2234	613	0.0620	0.0799	0.340
LC2022-iF2s	1.94	21776	1964	751	0.0697	0.0677	0.448

location to the corresponding wall in Lusher and Coleman [38], which is larger than the channel half-height above the isothermal wall, and smaller above the adiabatic wall. This treatment differs from the approach of Huang *et al.* [8], who used the channel half-height as the boundary layer thickness for both isothermal and adiabatic walls. Hence the values listed in table III and table IV are not exactly the same, but still close to that in Huang *et al.* [8]. Similar approach is used in the study of Guo *et al.* [49] on turbulent channel flow with a cold-wall/hot-wall setup.

Additionally, since not all datasets from Lusher and Coleman [38] provide the necessary information to compute ψ_3 , we only test the performance on cases with the required data, labeled as "iC, iD, iD2, iE, iE2s, iF2, iF2s" in table III. For more details, the reader can refer to Lusher and Coleman [38] and Huang *et al.* [8].

The temperature profiles for the isothermal wall side under VD-type and SL-type transformations are presented in Fig. 8 and 9. The transformations by Chen *et al.* [42], Huang *et al.* [8] and Cheng and Fu [35] are also plotted for comparison. Regarding this boundary condition, all transformations yield pronounced logarithmic profiles, with the SL-type transformations providing better collapse of the data in the buffer layer.

In particular, as shown in Fig. 9, the transformations by Chen *et al.* [42] and Huang *et al.* [8] provide an excellent data collapse and a clear logarithmic profile in the overlap layer. For the transformation by Cheng and Fu [35], the logarithmic slope remains uniform, but the magnitude exhibits relatively large variations across different cases. Such limitation on the isothermal wall

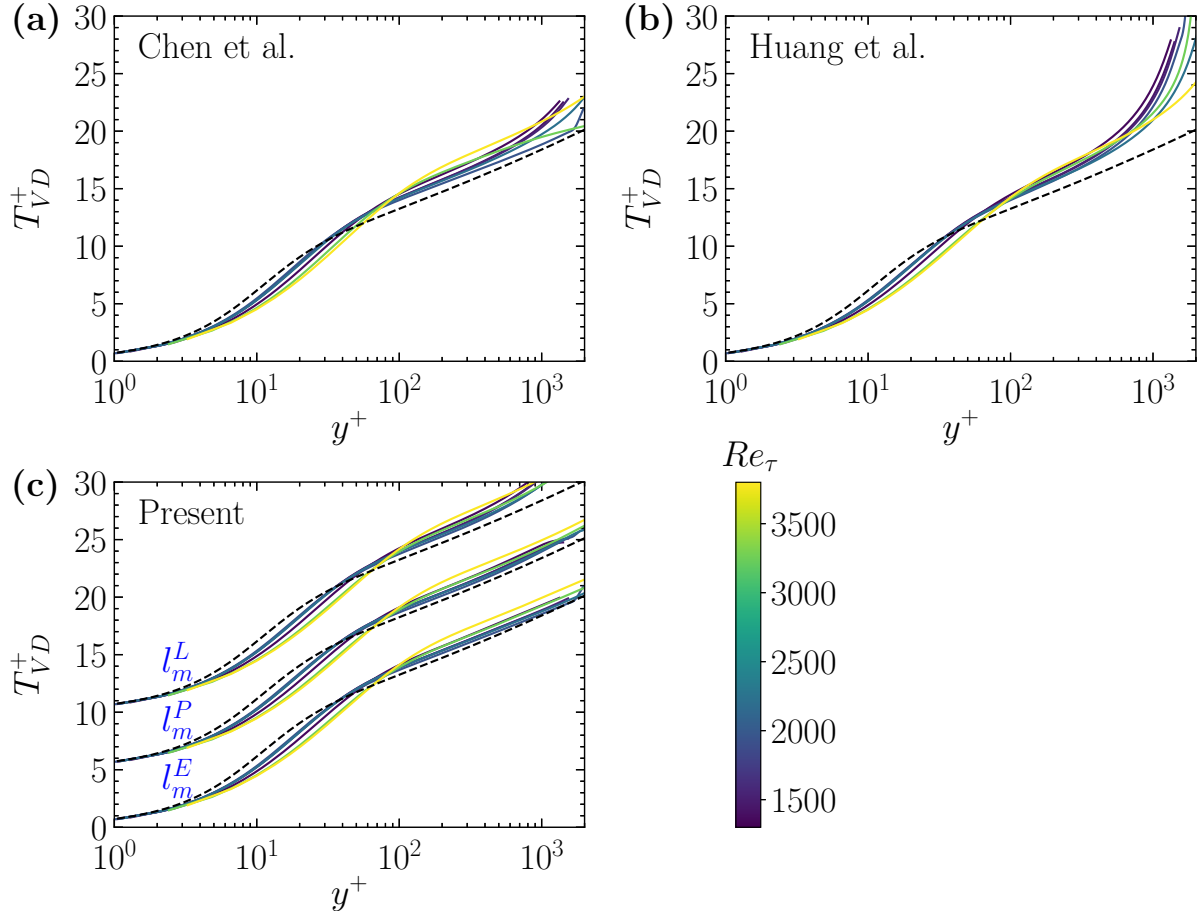


FIG. 8. Temperature profiles above the isothermal wall with mixed thermal configuration under the VD-type transformation of (a) Chen *et al.* [42], (b) Huang *et al.* [8], and (c) the present transformation given by Eq. (31), using DNS data from Lusher and Coleman [38]. Additional details are provided in table III. All subfigures share the same color bar. In panel (c), results from l_m^P and l_m^L are shifted upward by 5 and 10 units, respectively. The black dashed lines are the same as Fig. 4.

was also reported in their study. In our transformations, under the SL-type transformation, all three mixing length models recover the law of the wall. Analogous to the classical isothermal configuration, the parabolic model l_m^P retains the wake region, while the enhanced model l_m^E substantially extends the logarithmic profile. It should be noted that, in Fig. 9 (d), the black dashed line shows slightly higher values than T_{SL}^+ using l_m^E for $y^+ > 300$. This behavior can be explained by the same reasoning as in Fig. 5(d). The blue dotted line represents incompressible temperature profile at $Re_\tau \approx 550$, with the overall temperature distribution agreeing with cases "iE2s" and "iF2". The observed discrepancies may be attributed to differences in the thermal wall configuration and the

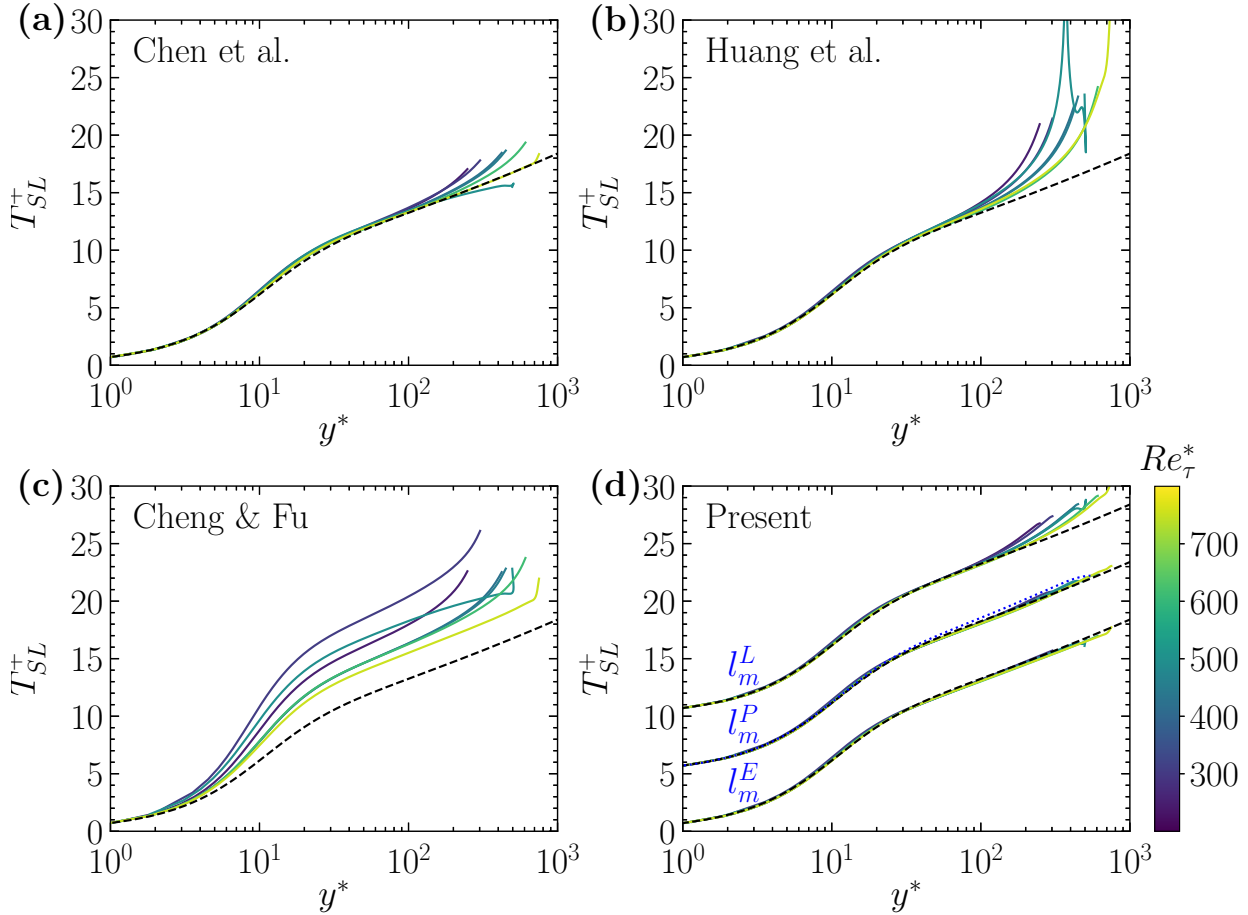


FIG. 9. Temperature profiles above the isothermal wall with mixed thermal configuration under the SL-type transformation of (a) Chen *et al.* [42], (b) Huang *et al.* [8], (c) Cheng and Fu [35], and (d) the present transformation given by Eq. (34), using DNS data from Lusher and Coleman [38]. Additional information are provided in table III. All subfigures share the same color bar. In panel (d), results from l_m^P and l_m^L are shifted upward by 5 and 10 units, respectively. The black dashed lines are the same as Fig. 4. The blue dotted line corresponds to incompressible case at $Re_\tau \approx 550$ from Pirozzoli *et al.* [15].

characteristic Reynolds number Re_τ^* . Note that small kinks and bends are observed near the edge of the boundary layer, which are likely related to the complex flow field in such mixed thermal configuration. We neglect this issue in the present study, without affecting the overall conclusion.

TABLE IV. Flow quantities on the adiabatic wall side of compressible turbulent channel flows under the mixed thermal configuration. The values are compatible with that of Lusher and Coleman [38] and Huang *et al.* [8].

Case	M_b	Re_b	Re_τ	Re_τ^*	M_τ	$-B_q$	\bar{T}_w/\bar{T}_e
LC2022-aC	2.25	9983	119	184	0.0654	0	1.435
LC2022-aD	1.70	13846	227	327	0.0561	0	1.355
LC2022-aD2	1.78	29024	401	585	0.0540	0	1.365
LC2022-aE	3.44	20638	134	220	0.0689	0	1.511
LC2022-aE2s	3.96	23770	254	595	0.0829	0	2.010
LC2022-aF2	1.86	45788	560	824	0.0524	0	1.380
LC2022-aF2s	1.94	47965	618	1038	0.0588	0	1.536

D. Performance above the adiabatic wall with mixed thermal boundary condition

Critical flow quantities on the adiabatic wall side are provided in table IV. The temperature profiles under VD-type and SL-type transformations are presented in figure 10 and 11. The transformations by Chen *et al.* [42], Huang *et al.* [8] and Cheng and Fu [35] are also plotted for comparison.

Unlike the isothermal boundary condition, temperature variation in the near-wall region above the adiabatic wall is minimal, suggesting only slight variations in density, dynamic viscosity, and thermal conductivity. As a result, the transformed temperature distribution in the viscous sublayer and buffer layer collapses well under all these transformations. In the overlap layer, the performance of transformations by Chen *et al.* [42] and Huang *et al.* [8] improves as Re_τ^* increases. The transformation by Cheng and Fu [35] yields similar behavior to those of Chen *et al.* [42], but shows closer agreement in magnitude. Our transformations collapse the profiles across the entire boundary layer, with the logarithmic profile extending into the channel center when using l_m^E . However, the slope with the enhanced mixing length model is slightly smaller than the reference profile in the wake region.

The most pronounced difference for the adiabatic wall lies in the magnitude, which is noticeably larger than the incompressible temperature profile. Actually, this overprediction begins from the viscous sublayer. Within our transformation framework, it is likely caused by an overpredic-

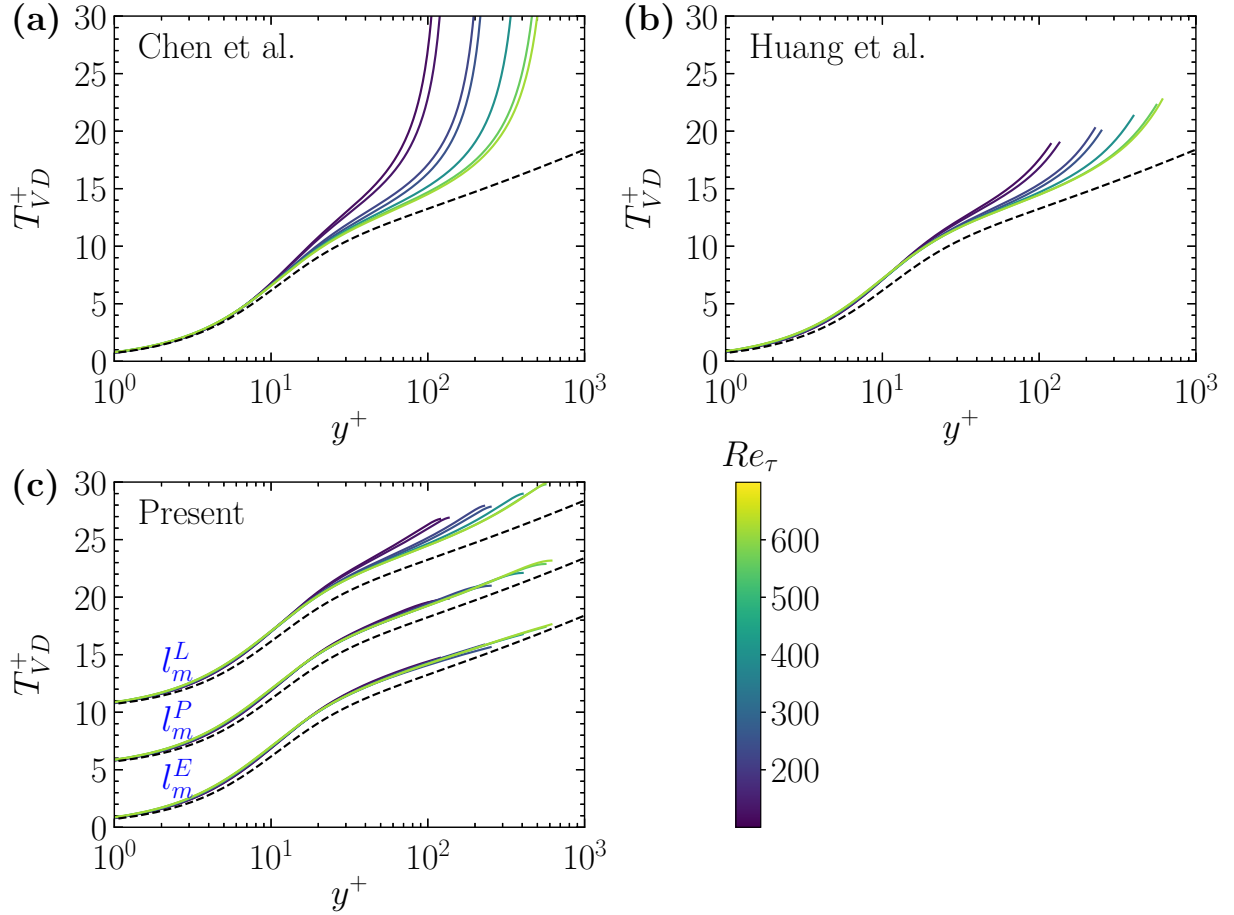


FIG. 10. Temperature profiles above the adiabatic wall with mixed thermal configuration under the VD-type transformation of (a) Chen *et al.* [42], (b) Huang *et al.* [8], and (c) the present transformation given by Eq. (31), using DNS data from Lusher and Coleman [38]. Additional information are provided in table IV. All subfigures share the same color bar. In panel (c), results from l_m^P and l_m^L are shifted upward by 5 and 10 units, respectively. The black dashed lines are the same as Fig. 4.

tion of l_m in the viscous sublayer and buffer layer on the adiabatic wall side. In addition, this discrepancy may also arise from differences in thermal boundary configurations, as the reference incompressible temperature profile is obtained from symmetric configuration rather than mixed one [15].

An exception is the SL-type transformation by Cheng and Fu [35], which exhibits the correct magnitude with increasing Reynolds number. Cheng and Fu [35] also concluded that this transformation performs well for the adiabatic wall.

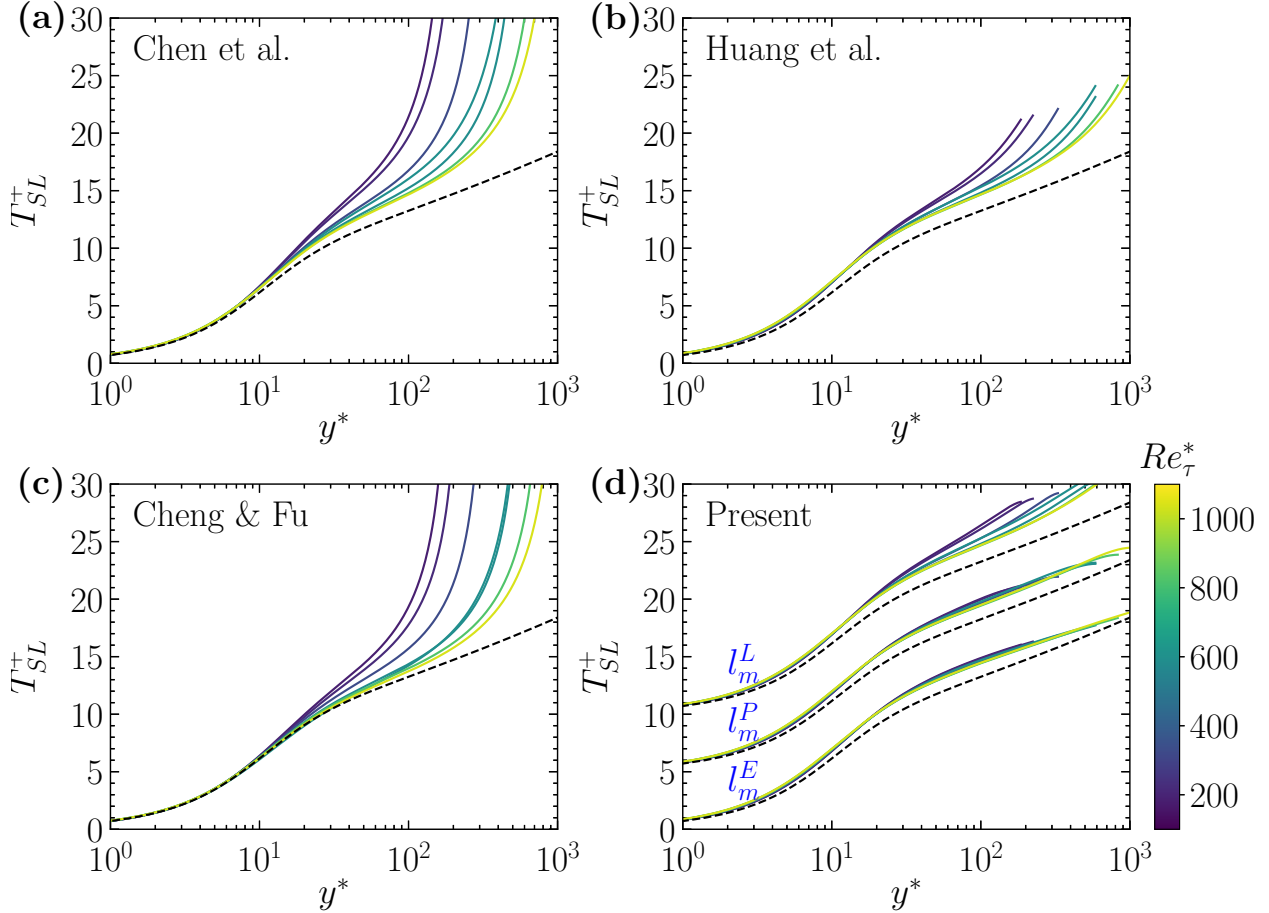


FIG. 11. Temperature profiles above the adiabatic wall with mixed thermal configuration under the SL-type transformation of (a) Chen *et al.* [42], (b) Huang *et al.* [8], (c) Cheng and Fu [35], and (d) the present transformation given by Eq. (34), using DNS data from Lusher and Coleman [38]. Additional information are provided in table IV. All subfigures share the same color bar. In panel (d), results from l_m^P and l_m^L are shifted upward by 5 and 10 units, respectively. The black dashed lines are the same as Fig. 4.

E. Diagnostic function

To assess the presence of logarithmic profile, the diagnostic is applied:

$$\Xi = y^+ \frac{dT_{VD}^+}{dy^+} \approx \text{const} \quad \text{or} \quad \Xi = y^* \frac{dT_{SL}^+}{dy^*} \approx \text{const.} \quad (53)$$

In principle, Ξ should remain constant ($\Xi = Pr_t/\kappa \approx 2.073$) within the logarithmic region. However, this requirement is quite strict under finite Reynolds number conditions [70], hence some deviation from constancy is expected.

Fig. 12 shows the Ξ profile for T_{SL}^+ under different boundary conditions and various SL-type

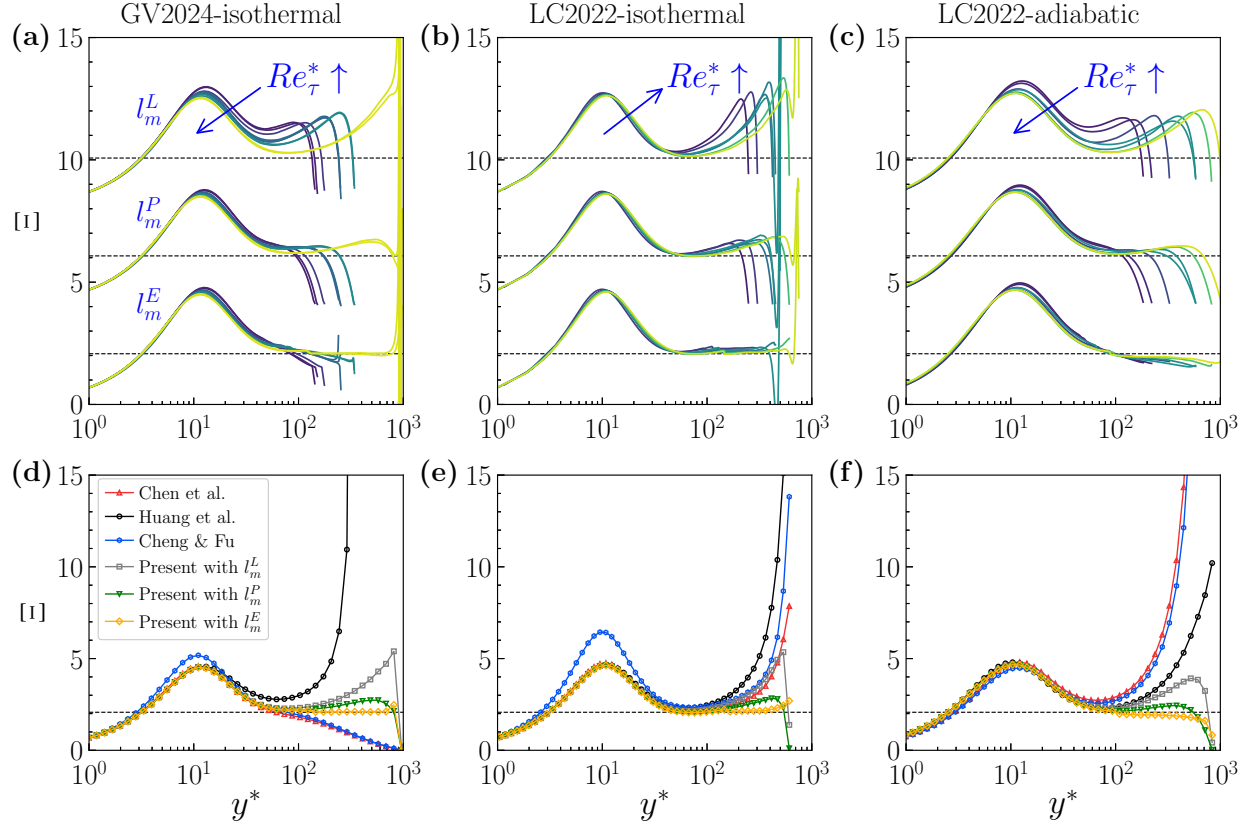


FIG. 12. Diagnostic function for different boundary conditions and various SL-type transformations. (a, b, c) represents our SL-type transformation using three different mixing length models for (a) GV2024-isothermal, (b) LC2022-isothermal, and (c) LC2022-adiabatic, respectively. (d, e, f) represent the Ξ under various SL-type transformations at three flow conditions: (d) GV2024 at $M_b = 1.57$, $Re_b = 25216$, and $Re^* = 965$ with isothermal, (e) LC2022-iF2 at $M_b = 1.86$, $Re_b = 20813$, and $Re^* = 613$ for the isothermal wall side, and (f) LC2022-aF2 at $M_b = 1.86$, $Re_b = 20813$, and $Re^* = 824$ for the adiabatic wall side. The dashed line represents the reference value, $\Xi = Pr_t/\kappa \approx 2.073, 6.073$, and 10.073 .

transformations. As seen in panels (a, b, c), when using the parabolic model l_m^P and the enhanced model l_m^E , Ξ collapses well in the inner layer across all three boundary conditions. Noticeable scatter is observed in the overlap layer for the linear model l_m^L , as shown in panels (a) and (c). Compared to l_m^L and l_m^P , the enhanced model l_m^E yields a broader range over which Ξ remains close to the reference value. As the Reynolds number increases, this region becomes more pronounced.

The kinks and bends near the channel center are likely due to DNS inaccuracies and deficiency of the mixing length models. Since they occur over a narrow region, we neglect this issue. For the adiabatic wall side, as shown in panel (c), the enhanced model results in relatively smaller Ξ

values than the reference.

Further more, for each boundary condition, we select one case with relatively high Reynolds number and compare the Ξ profile across different transformations, as shown in panels (d, e, f). Our transformation yields a significantly broader logarithmic region than the other three transformations, particularly when l_m^P and l_m^E are applied.

To summarize the previous sections, the results show that both VD-type and SL-type transformations, as defined in Eqs. (31) and (34), successfully collapse the temperature distribution above isothermal and adiabatic walls. The SL-type transformation demonstrate better performance and also recovers the law of the wall for temperature. The diagnostic function is also well collapsed in viscous sublayer and buffer layer, and remains close to the reference value in the outer layer. The parabolic mixing length model retains the wake profile, while the enhanced model collapses the entire outer layer, leading to extended logarithmic profile. Slight variations in the logarithmic intercept (B_T) are observed across different boundary conditions. For comparison, we also presented the results under the transformations of Chen *et al.* [42], Huang *et al.* [8], and Cheng and Fu [35], which demonstrate improved performance with increasing Re_τ^* . These transformations are expected to recover the law of the wall at sufficiently high Reynolds numbers.

IV. ANALYSIS

In Eqs. (31) and (34), three parameters (ψ_1 , ψ_2 , and ψ_3) are introduced, distinguishing these transformations from those of Huang *et al.* [8]. In this section, we examine the roles of ψ_1 , ψ_2 , and ψ_3 and demonstrate that their mechanisms stem from the damping effects in the transformation. This analysis here justifies the inclusion and exclusion of the parameters depending on the thermal wall conditions. Consequently, simplified temperature transformations are presented for the classical isothermal wall configuration. Furthermore, the application of the proposed transformation in near-wall modeling and its extension to more general configurations are discussed.

A. Damping effects of ψ_1 , ψ_2 and ψ_3

Fig. 13(a) presents the temperature profile under the SL-type transformation with different combinations of ψ_1 , ψ_2 , and ψ_3 for the case at $M_b = 1.7$ and $Re_b = 10000$. The profiles of ψ_1 , ψ_2 , and ψ_3 across the channel are also shown in Fig. 13(b). For clarity, one can directly

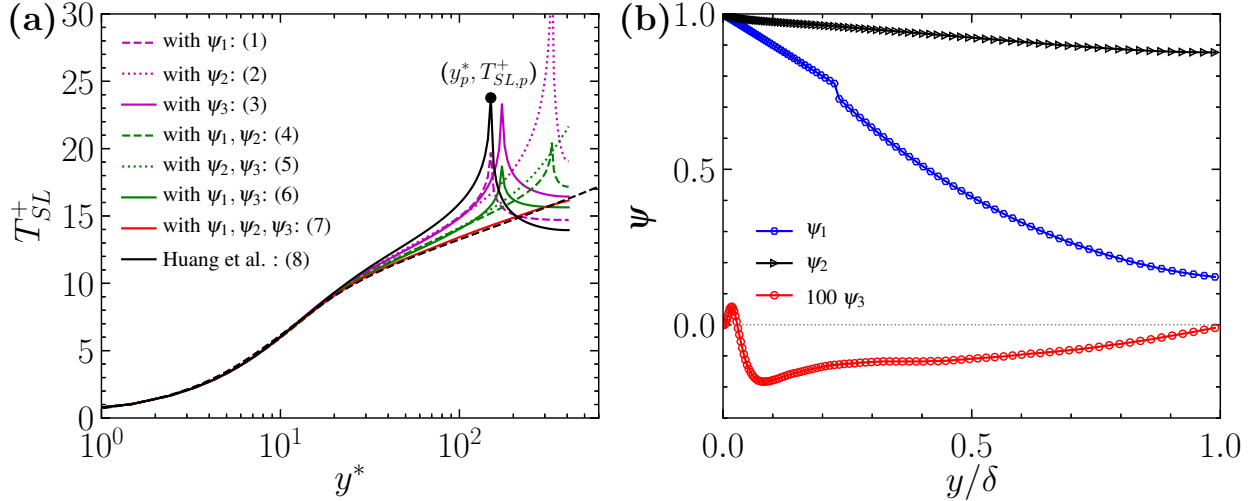


FIG. 13. Influence of ψ_1 , ψ_2 , ψ_3 for the case at $M_b = 1.7$ and $Re_b = 10000$, see table II. (a) T_{SL}^+ profile for different combinations of ψ_1 , ψ_2 , and ψ_3 . (b) Distributions of ψ_1 , ψ_2 , and ψ_3 . Each curve in (a) is labeled with a number. In the legend, the label "with $\psi_i (i = 1, 2, 3)$ " indicates that the corresponding parameter is active. When any of $\psi_i (i = 1, 2, 3)$ is inactive, the default values $\psi_1 = 1.0$, $\psi_2 = 1.0$, and $\psi_3 = 0$ are applied. Curve (8) represents the SL-type transformation of Huang *et al.* [8], given by Eq. (B4), where none of ψ_1 , ψ_2 , or ψ_3 are active and all take their default values. The enhanced mixing length model l_m^E , given by Eq. (44), is employed to compute ψ_1 in curves (1), (4), (6), and (7). The black dashed lines are the same as Fig. 4.

follow the sequence (8) \rightarrow (1) \rightarrow (4) \rightarrow (7), which illustrates how the profile transitions from the transformation by Huang *et al.* [8] to that of our new transformation. The best performance is achieved in curve (7), where all the three parameters are active.

The influence of ψ_1 is determined by comparing curve (5) with (7) in panel (a). Outside the buffer layer, curve (7) consistently presents a smaller slope and magnitude than curve (5). This behavior is attributed to the damping effect of ψ_1 . In the transformation of Huang *et al.* [8], ψ_1 remains constant at 1.0 throughout the channel. However, as shown in panel (b), ψ_1 in our transformation decreases from 1.0 at the wall to approximately 0.16 at the channel centerline, directly damping the integrand and leading to a lower transformed temperature. Similar behaviors are observed when comparing curves (2) with (4) and (3) with (6).

To determine the influence of ψ_2 , we examine curves (1), (3), (6), and (8), where ψ_2 is inactive, resulting in a significant spike. This behavior is directly caused by the sign change in the denominator of Eqs. (31) and (34). To illustrate this, we focus on curve (8), which corresponds to the

transformation by Huang *et al.* [8]. Comparing Eqs. (24) and (27), we obtain:

$$(B_q + \psi_2(\gamma-1)M_\tau^2 u^+ + \psi_3) \propto q_w - \left(\psi_2 \tau_w \tilde{u} - \overline{\rho v'' \frac{1}{2} u_i'' u_i''} \right). \quad (54)$$

We define $q_y = \psi_2 \tau_w \tilde{u} - \overline{\rho v'' \frac{1}{2} u_i'' u_i''}$. In our transformation, q_y includes the molecular and turbulent diffusion of kinetic energy across the y -plane, and the work of the external body force below it. However, in the transformation by Huang *et al.* [8], the total shear stress is assumed to be equal to the wall shear stress, and the effects of the body force and the TKE transport are neglected. As a result, the following equation holds:

$$(B_q + (\gamma-1)M_\tau^2 u^+) \propto (q_w - \tau_w \tilde{u}). \quad (55)$$

This simplification indicates $q_y = \tau_w \tilde{u}$. We point out that it is this simplification that directly leads to the peak point $(y_p^*, T_{SL,p}^+)$ in curve (8). Here, y_p^* corresponds to the location where $\tilde{u} = u_b$. Actually, for the density based body force, the overall energy balance of the whole channel satisfies $q_w = \tau_w u_b$ [71]. For the volume based body force, this relation still holds approximately. Applying $q_y = \tau_w \tilde{u}$ results in $|q_y| < |q_w|$ for $y < y_p$, since $\tilde{u} < u_b$, and $|q_y| > |q_w|$ for $y > y_p$, because $\tilde{u} > u_b$. As a result, the sign of the denominator changes across this location, leading to the peak value of T_{SL}^+ in curve (8). The same reasoning applies to curves (1), (3) and (6).

As for the influence of ψ_3 , a similar but significantly more narrow spike is also observed in curves (2) and (4), where ψ_2 is active but ψ_3 is not. This behavior arises for the same reason as the spike caused by ψ_2 . Since the magnitude of $\psi_2(\gamma-1)M_\tau^2 u^+$ is typically much larger than ψ_3 , the spike caused by ψ_2 generally affects a greater proportion of the channel, whereas the spike caused by ψ_3 is considerably delayed and confined to a narrow region near the channel center.

When both ψ_2 and ψ_3 are active, the spike is effectively eliminated, as shown in curves (5) and (7). From Fig. 13(b), we observe that ψ_2 decreases from 1 at the wall to approximately 0.85 at the channel centerline, effectively damping the second term $\psi_2(\gamma-1)M_\tau^2 u^+$. In the outer layer, ψ_3 is always negative and has the same sign as B_q , providing a damping effect to the whole integration of the transformation, thereby preventing a sign change. Consequently, the overall behavior stabilizes, eliminating the spike.

As we approach the channel center, the magnitude of both sides of Eq. (54) decreases. A limited energy imbalance could trigger the sign change in the denominator, consequently leading to a spike, which differs significantly from the situation in velocity transformations.

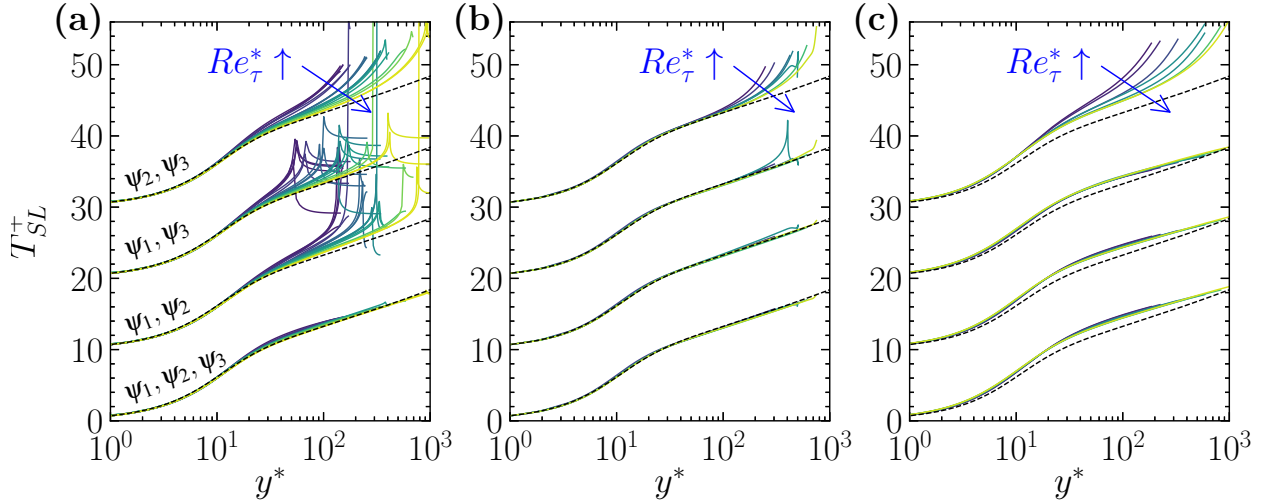


FIG. 14. Transformed temperature profiles in the absence of ψ_1 , ψ_2 , and ψ_3 under SL-type transformation. (a) The classical isothermal wall configuration (see table I and II). (b) Isothermal wall side for the mixed thermal configuration (see table III). (c) Adiabatic wall side (see table IV). The first group of curves in the bottom of each panel indicates the complete transformation with all of ψ_1 , ψ_2 , and ψ_3 activated. The other three groups of curves correspond to neglecting one of the three parameters, and are shifted upward by multiples of 10 units. The black dashed lines are the same as Fig. 4.

Regarding the mixed isothermal/adiabatic configuration, we can make the same analysis (the results are not shown here for simplicity). Compared to the classical isothermal wall configuration, there are two distinct characteristics in mixed thermal condition. First, the thermal energy is removed exclusively from the isothermal wall side, making q_w approximately twice as large as that in the classical configuration. However, the shear stress and velocity in the channel do not increase proportionally. Consequently, the sign of denominator in the transformation of Huang *et al.* [8] remains unchanged and no spikes are observed. Second, as shown in Fig. 2(b, c), the turbulent heat conduction component q_T^t makes a significantly larger contribution to the total energy balance, and it does not decrease to zero near the channel center, in contrast to the classical configuration. As introduced in Sec. II C, q_k^t is significantly smaller than q_T^t under this configuration. Therefore, it is expected that ψ_3 can be neglected accordingly. In addition, q_f is also smaller than q_T^t in the majority of the channel, suggesting a less significant role of ψ_2 .

The above analysis can be validated through Fig. 14, which presents the transformed temperature profiles in the absence of ψ_1 , ψ_2 , and ψ_3 under SL-type transformation using l_m^E . The first group of curves in the bottom of each panel correspond to the complete transformation with all

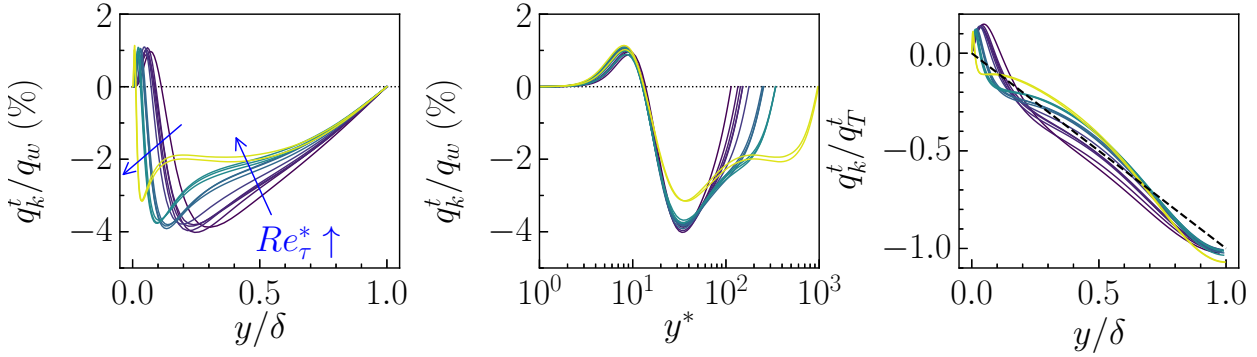


FIG. 15. Profile of TKE transport (q_k^t) in compressible turbulent channel flow with the classical isothermal configuration. (a) q_k^t/q_w versus y/h , (b) q_k^t/q_w versus y^* , and (c) q_k^t/q_T^t versus y/h . See table I for details of the DNS dataset.

three parameters activated. As shown in panel (a), for the classical isothermal wall configuration, the exclusion of any of ψ_1 , ψ_2 , and ψ_3 makes significant difference, suggesting that they are all important. Particularly, excluding either ψ_2 or ψ_3 would result in the kinks. In mixed thermal configuration, ψ_1 is the most important parameter for both isothermal and adiabatic wall sides, while ψ_2 and ψ_3 make insignificant difference. However, this does not imply that the body force is unimportant in turbulent channel flow.

B. Modeling the TKE transport term

Analogous to the complete-form transformations by Chen *et al.* [42] and Cheng and Fu [35], the inclusion of TKE transport term, $q_k^t = -\overline{\rho v'' \frac{1}{2} u_i'' u_i''}$, adds complexity to the proposed transformation, which is a weakness. A practical challenge also arises because many open-source DNS databases do not provide this third-order statistics, making the validation of our transformations difficult on such datasets.

As demonstrated in Sec. IV A, the TKE transport can be safely neglected in mixed thermal wall configuration, while should be retained in classical isothermal wall setup. To eliminate the dependence on q_k^t , two approaches have been applied in previous studies. Huang *et al.* [8] and Cheng and Fu [35] used $q_y = \tau_w \tilde{u}$ based on the constant stress assumption. Chen *et al.* [42] applied $q_y = \tau_{xy} \tilde{u}$ to derive a simplified version of their transformation, where $\tau_{xy} = (\bar{\mu} + \bar{\mu}_t) d\tilde{u}/dy$ represents the total shear stress. Both methods neglect the influence of the external body force. A third option would be to model the TKE transport q_k^t rather than q_y .

Fig. 15 presents the profiles of q_k^t in three different forms, using DNS data from Gerolymos and Vallet [60, 61, 62] (see table I). The distribution of q_k^t/q_w , shown in panel (a), is strongly influenced by Mach and Reynolds numbers. Plotting the profile with respect to y^* helps to collapse the distribution in the near wall region, as shown in panel (b), which is consistent with the findings of Duan *et al.* [34, 72] and Cogo *et al.* [73]. There exists a critical location, $y_k^* \approx 13.5$, where the TKE transport changes direction: towards the wall for $y^* < y_k^*$ and towards the channel centerline for $y^* > y_k^*$. However, the profiles do not collapse well in the logarithmic and wake regions when plotted against y^* . In Sec. II C, we point out that the turbulent diffusion of thermal energy (q_T^t) should serve as the basis when evaluating the relative importance of each term in Eq. (23) within the overlap layer. This motivates the normalization by q_T^t shown in panel (c). It exhibits good overall collapse across the entire channel. The following relation can be applied:

$$q_k^t = \beta \left(\frac{y}{h} \right) q_T^t. \quad (56)$$

The distribution of β varies with flow conditions and appears to be primarily influenced by Re_τ^* . As shown by the black dashed line in Fig. 15(c), the estimate can be expressed as:

$$\beta \left(\frac{y}{h} \right) \approx -\frac{y}{h}. \quad (57)$$

Invoking Eqs. (56) and (57) into Eq. (24) and following the same approach in Sec. II C, we obtain the simplified versions of the VD-type and SL-type transformations for the classical isothermal wall configuration:

$$T_{VD,m}^+ = \int_0^{\theta^+} \frac{\psi_1(1+\beta)}{B_q + \psi_2(\gamma-1)M_\tau^2 u^+} \sqrt{\rho^+} d\theta^+, \quad (58)$$

$$T_{SL,m}^+ = \int_0^{\theta^+} \frac{\psi_1(1+\beta)}{B_q + \psi_2(\gamma-1)M_\tau^2 u^+} \sqrt{\rho^+} \left(1 + \frac{1}{2} \frac{y^+}{\rho^+} \frac{d\rho^+}{dy^+} - \frac{y^+}{\mu^+} \frac{d\mu^+}{dy^+} \right) d\theta^+. \quad (59)$$

Compared to the complete forms in Eqs. (31) and (34), ψ_3 in the denominator is replaced by $(1+\beta)$ in the numerator with β given by Eq. (57), thereby removing the direct reliance on high-order statistics while still retaining its effect.

Since the publicly available DNS datasets of Trettel and Larsson [21], Modesti and Pirozzoli [33], and Yao and Hussain [74] do not contain the TKE transport, they cannot be used to validate the transformations in Eqs. (31) and (34). However, these datasets are suitable for validating the simplified transformations in Eqs. (58) and (59). Fig. 16 presents the transformed temperature profiles $T_{VD,m}^+$ and $T_{SL,m}^+$. The results from the DNS of Gerolymos and Vallet [60, 61, 62] are also included.

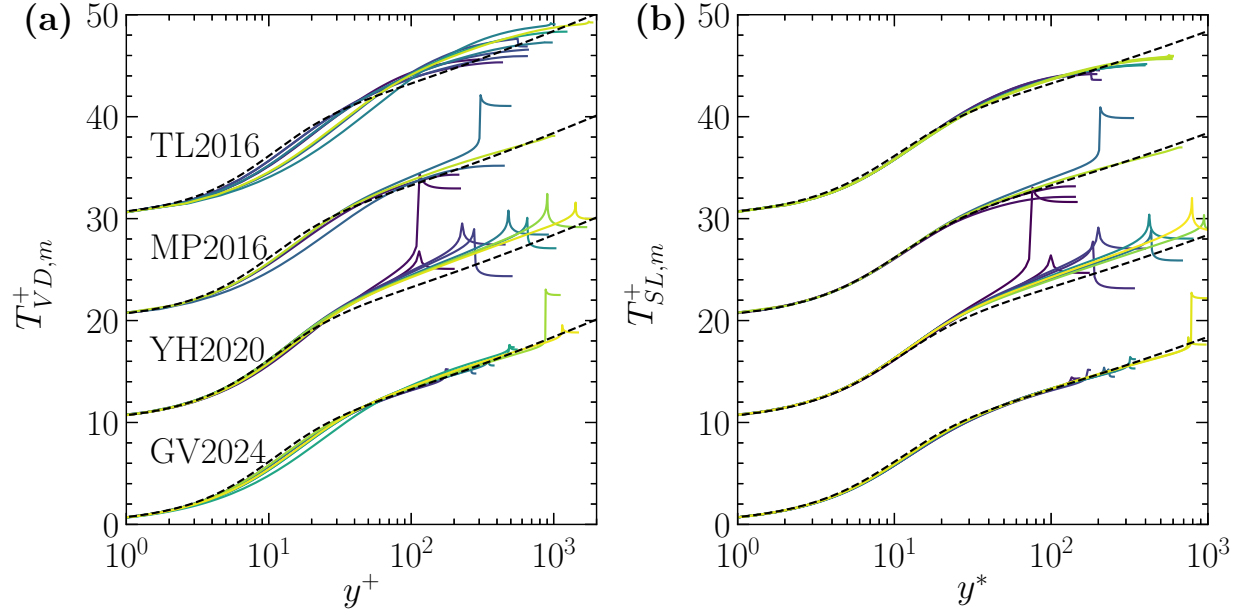


FIG. 16. Transformed temperature profiles under the simplified VD-type (a) and SL-type (b) transformations in Eqs. (58) and (59) using DNS data from Trettel and Larsson [21], Modesti and Pirozzoli [33], Yao and Hussain [74], and Gerolymos and Vallet [60, 61, 62], respectively. They are labeled as "TL2016", "MP2016", "YH2020", and "GV2024", and are shifted upward by multiple 10 units. The enhanced mixing length model l_m^E is applied to compute ψ_1 . The black dashed lines are the same as Fig. 4.

As shown, the simplified transformations yield satisfactory results, with the SL-type transformation showing good agreement with the incompressible temperature distribution in the inner layer, particularly at high Reynolds numbers. An exception is the transformed results based on the DNS from Yao and Hussain [74], which exhibits a relatively higher magnitude and a less well-collapsed profile in the outer layer. We note that the temperature profiles (\tilde{T}/\tilde{T}_w) from Yao and Hussain [74] are slightly higher than those from Modesti and Pirozzoli [33] at the same Mach and Reynolds numbers. Such discrepancy may have contributed the reduced agreement observed here. Nevertheless, the disagreement remains small. The simplified VD-type transformation also yields relatively good collapse in the logarithmic region.

A series of kinks can be observed in the simplified transformation, particularly on the DNS data of Yao and Hussain [74]. As explained in Sec. IV A, this is due to the removal of ψ_3 from the denominator. In addition, the transformation of Huang *et al.* [8] yields similar results to those observed in Sec. III A using the DNS datasets of Trettel and Larsson [21], Modesti and Pirozzoli [33], and Yao and Hussain [74]. Therefore, they are not shown here for brevity.

These results demonstrate the effectiveness of the approximation for q_k^t and the simplified transformations given by Eqs. (58) and (59). However, it should be noted that Eq. (57) is only a coarse estimation. A more advanced model for q_k^t is required to further improve the performance of the simplified transformations. This is beyond the scope of present study and is left for future research.

C. Potential applications to near-wall modeling

Over the years, various approaches have been developed for near-wall modeling of turbulent flows [51, 75]. However, many of these methods encounter limitations when applied to compressible turbulent boundary layers. Knowledge from compressibility transformations, including both velocity and temperature transformations, can be leveraged to improve the performance of existing near-wall modeling techniques for compressible flows or to extend models originally developed for incompressible flows to compressible ones.

For example, in the studies by Hendrickson *et al.* [76, 77], the incompressible eddy viscosity is corrected using the velocity transformation kernel to model the compressible eddy viscosity. Following this idea, the temperature transformation could similarly be implemented to improve the modeling of compressible thermal eddy diffusivity. In the study of Chen *et al.* [36], the temperature transformation proposed by Cheng and Fu [35] is applied to remove the reliance on boundary-layer-edge quantities in the temperature-velocity relation. Additionally, Modesti and Pirozzoli [43] demonstrated that the velocity and temperature transformations can be applied inversely to reconstruct compressible mean profiles from their incompressible counterparts. Although their study focuses on low-Mach-number flows with variable properties, the same approach can be explored in high-speed compressible flows. Furthermore, wall models directly based on the log-law have been applied to incompressible wall modeling, such as the algebraic wall models [78–81] and the control-based approaches [82, 83]. It will be of great significance to develop wall models for compressible flows based on the log-law of transformed velocity and temperature profiles.

Based on the above analysis, the potential applications of the proposed temperature transformation are briefly discussed below.

First, in the case of large eddy simulation, the high-order term may be partially resolved. Accordingly, the transformation can be readily employed for wall-modelled large eddy simulation following the control-based approach proposed by Nicoud *et al.* [82]. The main difference is that both velocity and temperature transformations, along with a more advanced control strategy, are

required for compressible flows.

Second, the proposed transformation can be applied inversely to construct the mean profiles and key flow quantities of compressible flows, following a similar approach as used by Modesti and Pirozzoli [43]. More specifically, given the M_b and Re_b of the turbulent channel flow, the inverse transformation outputs the mean profiles of velocity, temperature, density, as well as key quantities including Re_τ , Re_τ^* , C_f , B_q , and \tilde{T}_c/\tilde{T}_w . Here, C_f and \tilde{T}_c are the friction coefficient and channel centerline temperature, respectively.

In this application, reference "incompressible" velocity and temperature profiles should be prescribed. For example, the compound incompressible velocity profile [53, 59] and the temperature profile [84, 85] can be used. A critical issue is the treatment of the high-order term in the transformation. In practice, it may be neglected by setting $\psi_3 \approx 0$ for high Reynolds numbers. Alternatively, the simplified transformation given in Eq. (59) may also be considered. As explained in Sec. IV A, neglecting ψ_3 leads to kinks and magnitude discrepancies in the transformed temperature profiles for the classical configuration, as shown in Fig. 14 (a). When applied inversely, these discrepancies propagate into the predicted mean compressible profiles. Consequently, the predicted mean temperature profile in the wake region is relatively lower than that obtained by employing the complete transformation. However, as Reynolds number increases, the kink shifts toward the channel centerline, and its influence on the predicted mean profiles and key flow quantities decreases accordingly. In such cases, using $\psi_3 \approx 0$ in the inverse transformation becomes a reasonable choice. Additionally, the accuracy of inverse transformation is also influenced by the accuracy of reference "incompressible" velocity and temperature profiles. In practice, prediction errors arising from neglecting ψ_3 and from inaccuracies in the "incompressible" reference profiles may either reinforce or partially cancel each other. Despite these concerns, our tests indicate that the predicted mean profiles and key quantities show reasonable agreement with the DNS results. Implementation details are outside the scope of the present study and will be reported in a separate manuscript.

Third, the transformation can also be incorporated in the classical wall-stress models in LES following the approach of Griffin *et al.* [58]. As shown in Fig. 14, when $\psi_3 \approx 0$ is applied, the transformed temperature profiles still approximately agree with the law of the wall at high Reynolds numbers in the inner layer. In such cases, $\psi_3 \approx 0$ might be reasonable when applied inversely in the wall model [58]. Moreover, as shown in Fig. 16(b), the simplified transformations in Eqs. (58) and (59) demonstrate reasonable agreement with the incompressible case within the

typical wall-modelled layer. Therefore, the simplified transformations may also be considered. Applications of these approaches in wall-modeled LES will be the subject of future investigation.

D. Extension to more general configurations

The present transformations are designed for compressible turbulent channel flows. They can potentially be extend to more general configurations that exhibit similar inner layer structure. However, appropriate adjustments of ψ_1 , ψ_2 , and ψ_3 are required.

For example, in zero pressure gradient boundary layer flows, the constant stress assumption approximately holds in the inner layer, indicating $\tau_{tot}^+ \approx 1$ in Eq. (28). One may also use $\tau_{tot}^+ = 1 - (y/\delta_e)^{1.5}$ [86, 87] for the entire boundary layer, where δ_e denotes the boundary layer thickness. At high Reynolds numbers, the commonly used linear model given in Eq. (42) can be readily applied. Nevertheless, we retain the flexibility to employ alternative models for ψ_1 when necessary. The influence of the body force term may also be neglected, which leads to $\psi_2 \approx 1$. Finally, the TKE transport term in ψ_3 , along with other high-order terms, should be carefully evaluated for different thermal wall conditions. Unfortunately, a model that accurately describe the high-order term distribution is not available. In addition, the cold wall configuration of compressible turbulent boundary layer flow leads to a non-monotonic temperature profile in the wall-normal direction. A local maximum appears in the buffer layer [88, 89], with $d\theta^+ < 0$ below this position and $d\theta^+ > 0$ above it. In such a case, it is considerably more challenging to develope the temperature transformation than in the turbulent channel flow. A more detailed investigation is left for future work.

V. CONCLUSION

In this study, VD-type and SL-type temperature transformations are proposed for compressible turbulent channel flow, as given in Eqs. (31) and (34). The effects of mixing length model, body force work, and TKE transport are incorporated through parameters ψ_1 , ψ_2 , and ψ_3 , respectively.

The proposed transformations are applicable to the classical isothermal wall and mixed isothermal/adiabatic wall configurations. The SL-type transformation yields better data collapse than the VD-type in the viscous sublayer and buffer layer, which is consistent with the findings of previous studies [8, 35, 41, 42], and aligns with conclusions drawn from velocity transformations [21–23].

The applied mixing length should satisfy $l_m \approx \kappa y$ to ensure $\psi_1 \approx 1$ in the viscous sublayer and account for the Reynolds stress in the overlap layer. In this case, the SL-type transformation is able to recover the compressible law of the wall. The commonly used linear model l_m^L yields the log-law only at high Reynolds numbers. When the parabolic model l_m^P is applied, the SL-type transformed temperatures agree with their incompressible counterparts at comparable Re_τ^* for the isothermal wall. Using the enhanced model l_m^E , both the VD-type and SL-type transformed temperature presents extended logarithmic behavior. Regarding the log-law, we obtain $B_T \approx 3.65$ with $\kappa = 0.41$ and $Pr_t = 0.85$ under the SL-type transformation at $Re_\tau^* \approx 1000$ for the classical isothermal wall configuration. As Re_τ^* increases, B_T is expected to decrease slightly.

The present study highlights the damping effects of ψ_1 , ψ_2 , and ψ_3 in the temperature transformations. For the mixed isothermal/adiabatic wall configuration, $\psi_2 = 1$ and $\psi_3 = 0$ can be valid approximations. For the classical isothermal wall configuration, accounting for TKE transport is essential. The approximation given in Eq. (57) removes direct reliance on this high-order term while still retaining its effect, as reflected in the simplified transformations in Eqs. (58) and (59). Nonetheless, the present study suggests a need for a more advanced model of the TKE transport term. While this study focuses on compressible turbulent channel flow, the proposed transformation may be extended to more general configurations. Such an extension would require more advanced models for ψ_1 , ψ_2 , and ψ_3 .

ACKNOWLEDGMENTS

The first author gratefully acknowledges financial support from the China Scholarship Council (No.202006320042). He also acknowledges insightful discussions with Dr. Deniz A. Bezgin and Mr. Aaron B. Buhendwa regarding simulations of turbulent channel flow using JAX-Fluids. Special thanks go to Prof. G. N. Coleman for his critical suggestions on implementing their DNS data.

AUTHOR DECLARATIONS

Conflict of Interest

The authors have no conflicts to disclose.

Author Contributions

Youjie Xu: Conceptualization (lead); Data curation (lead); Formal analysis (lead); Investigation (lead); Methodology (lead); Software (lead); Validation (lead); Visualization (lead); Writing-original draft (lead). **Steffen J. Schmidt:** Funding acquisition (equal); Project administration (equal); Resources (equal); Supervision (equal); Writing-review & editing (equal). **Nikolaus A. Adams:** Funding acquisition (equal); Project administration (equal); Resources (equal); Supervision (equal); Writing-review & editing (equal).

DATA AVAILABILITY STATEMENT

The DNS data that used as reference in this study are available in the cited literature. The wall-resolved large eddy simulation data are available from the corresponding author upon reasonable request.

AUTHOR ORCID.

Youjie Xu <https://orcid.org/0009-0006-8445-3200>;

Steffen J. Schmidt <https://orcid.org/0000-0001-6661-4505>;

Nikolaus A. Adams <https://orcid.org/0000-0001-5048-8639>.

Appendix A: Derivation of \tilde{u}_b^i/\tilde{u}

When implementing the transformations in Eqs. (31) and (34), we need to compute \tilde{u}_b^i/\tilde{u} in ψ_2 . Its value at the wall is derived below.

Recall the definition in Eq. 21, we obtain:

$$\lim_{y \rightarrow 0} \frac{\tilde{u}_b^i(y)}{\tilde{u}(y)} = \lim_{y \rightarrow 0} \frac{1}{y\tilde{u}(y)} \int_0^y \tilde{u}(\eta) d\eta. \quad (\text{A1})$$

In the viscous sublayer, the velocity follows a linear profile, i.e., $\tilde{u} = Cy$, where C is a constant. Thus, we get:

$$\int_0^y \tilde{u}(\eta) d\eta = \int_0^y C\eta d\eta = C\frac{y^2}{2}. \quad (\text{A2})$$

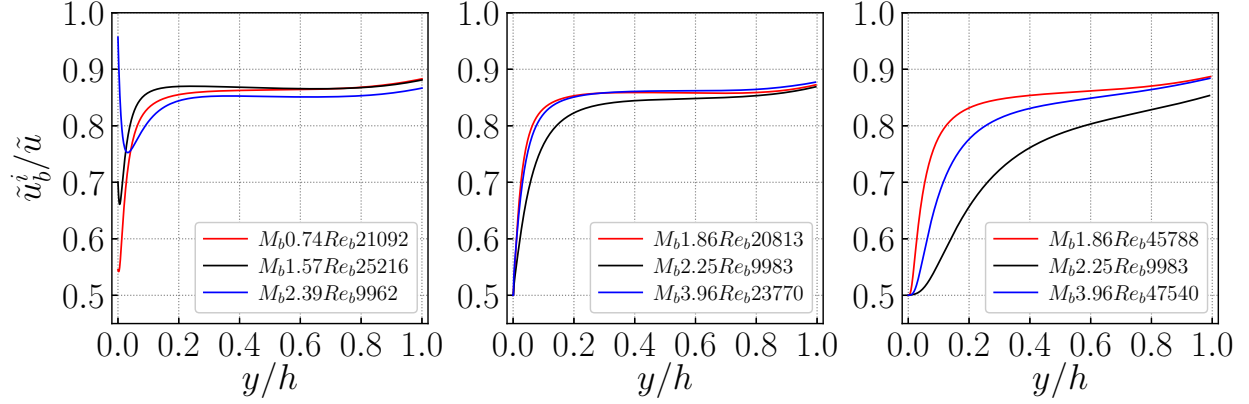


FIG. 17. Profiles of \tilde{u}_b^i/\tilde{u} under different body force configurations. (a) Density-based body force, computed using Eq. (50) and DNS data from Gerolymos and Vallet [60, 61, 62]. (b) Volume-based body force, computed using Eq. (21) and DNS data from Lusher and Coleman [38], isothermal wall side. (c) Volume-based body force, computed using Eq. (21) and DNS data from Lusher and Coleman [38], adiabatic wall side.

Finally, we obtain \tilde{u}_b^i/\tilde{u} at the wall:

$$\left. \frac{\tilde{u}_b^i}{\tilde{u}} \right|_w = \lim_{y \rightarrow 0} \frac{\tilde{u}_b^i(y)}{\tilde{u}(y)} = \lim_{y \rightarrow 0} \frac{Cy^2/2}{Cy^2} = \frac{1}{2}. \quad (\text{A3})$$

Similarly, for density-based body force, we use the following equation to approximate the value at the wall:

$$\left. \frac{\tilde{u}_b^{i,\rho}}{\tilde{u}} \right|_w = \lim_{y \rightarrow 0} \frac{\tilde{u}_b^i(y)}{\tilde{u}(y)} = \frac{1}{2} \frac{\bar{\rho}_w}{\rho_b}. \quad (\text{A4})$$

Representative distributions of \tilde{u}_b^i/\tilde{u} under different body force and thermal configurations are presented in Fig. 17. It can be observed that $\tilde{u}_b^i/\tilde{u} = 0.5$ at $y = 0$ for the volume-based body force. In contrast, for the density-based body force, the value at the wall increases with increasing Mach numbers. In the vicinity of channel center, the values are similar across the three configurations. Above the adiabatic wall, the ratio increases more slowly than above the isothermal wall.

Appendix B

The VD-type and SL-type transformations by Chen *et al.* [42], originally presented in Eq. (5.1) and (5.2) of their paper, are rewritten here for convenience.

$$T_{VD}^{+,Chen} = \int_0^{\theta^{Chen}} \frac{d\theta^{Chen}}{\theta_{\tau,c}^*}. \quad (\text{B1})$$

$$T_{SL}^{+,Chen} = \int_0^{\theta^{Chen}} \left(1 + \frac{y}{Re_\tau^*} \frac{dRe_\tau^*}{dy} \right) \frac{d\theta^{Chen}}{\theta_{\tau,c}^*}. \quad (B2)$$

Here, $\theta^{Chen} = \tilde{T}_w - \tilde{T}$, $Re_\tau^* = \bar{\rho} \sqrt{\tau_w / \bar{\rho} h / \bar{\mu}}$, $\theta_{\tau,c}^* = (q_w^{Chen} + \bar{q}^{Chen}) / (\bar{\rho} c_p u_\tau^*)$, $u_\tau^* = \sqrt{\tau_w / \bar{\rho}}$, $\bar{q}^{Chen} = \overline{\sigma_{i2} u_i} + \overline{\sigma'_{i2} u'_i} - \overline{\rho v'' u''_i} \tilde{u}_i - \overline{\rho v'' \frac{1}{2} u''_i u''_i}$, and q_w^{Chen} represents the wall heat flux in the same direction of wall-normal coordinate.

The VD-type and SL-type transformations by Huang *et al.* [8], originally presented in Eq. (4.6) and (5.6) of their paper, are rewritten here for convenience.

$$T_{VD}^{+,Huang} = \int_0^{\theta^{Huang}} \frac{1}{B_q + (\gamma - 1)M_\tau^2 u^+} \sqrt{\frac{\bar{\rho}}{\bar{\rho}_w}} d\theta^{Huang}. \quad (B3)$$

$$T_{SL}^{+,Huang} = \int_0^{\theta^{Huang}} \frac{1}{B_q + (\gamma - 1)M_\tau^2 u^+} \sqrt{\frac{\bar{\rho}}{\bar{\rho}_w}} \left(1 + \frac{1}{2} \frac{y^+}{\bar{\rho}} \frac{\partial \bar{\rho}}{\partial y^+} - \frac{y^+}{\bar{\mu}} \frac{\partial \bar{\mu}}{\partial y^+} \right) d\theta^{Huang}. \quad (B4)$$

Here, $\theta^{Huang} = (T_w - T) / T_w$. The definition of B_q and M_τ are the same as those in Sec. II.

Cheng and Fu [35] originally proposed two types of semi-local transformations depending on the high-order term is neglected or not, see Eq. (22) and (30) of their paper. For comparison, we select the complete form and rewrite it in the following equation:

$$T_{SL}^{+,Cheng} = \int_0^{\theta^{+,Cheng}} \frac{\sqrt{\bar{\rho}^+}}{1 - \frac{q_w^{Cheng}}{q_w}} d\theta^{+,Cheng}. \quad (B5)$$

Here, $\theta^{+,Cheng} = (T - \bar{T}_w) / \theta_\tau$ with $\theta_\tau = q_w / (\bar{\rho}_w c_p u_\tau)$, $\bar{\rho}^+ = \bar{\rho} / \bar{\rho}_w$, and $\bar{q}^{Cheng} = \overline{u \tau_{xy}} - \overline{\rho \tilde{u} u'' v''} - \overline{\rho v'' \frac{1}{2} u'' u''}$. Note that q_w^{Cheng} represents the heat flux removed from the wall.

[1] J. P. Slotnick, A. Khodadoust, J. J. Alonso, D. L. Darmofal, W. Gropp, E. A. Lurie, and D. J. Mavriplis, *CFD Vision 2030 Study: A Path to Revolutionary Computational Aerosciences*, Tech. Rep. NASA/CR-2014-218178 (NASA, 2014).

[2] K. A. Goc, O. Lehmkuhl, G. I. Park, S. T. Bose, and P. Moin, Large eddy simulation of aircraft at affordable cost: A milestone in computational fluid dynamics, *Flow* **1**, E14 (2021).

- [3] R. Stoll, J. A. Gibbs, S. T. Salesky, W. Anderson, and M. Calaf, Large-Eddy Simulation of the Atmospheric Boundary Layer, *Boundary-Layer Meteorology* **177**, 541 (2020).
- [4] J. N. Sørensen, Aerodynamic aspects of wind energy conversion, *Annual Review of Fluid Mechanics* **43**, 427 (2011).
- [5] S. Pope, *Turbulent Flows* (Cambridge University Press, 2000).
- [6] H. Tennekes and J. L. Lumley, *A First Course in Turbulence* (MIT Press, Cambridge, MA, 1972).
- [7] P. Bradshaw and G. P. Huang, The law of the wall in turbulent flow, *Proceedings of the Royal Society of London. Series A: Mathematical and Physical Sciences* **451**, 165 (1995).
- [8] P. Huang, G. Coleman, P. Spalart, and X. Yang, Velocity and temperature scalings leading to compressible laws of the wall, *Journal of Fluid Mechanics* **977**, A49 (2023).
- [9] M. Lee and R. D. Moser, Direct numerical simulation of turbulent channel flow up to $Re\tau \approx 5200$, *Journal of Fluid Mechanics* **774**, 395 (2015).
- [10] S. Hoyas, M. Oberlack, F. Alcántara-Ávila, S. V. Kraheberger, and J. Laux, Wall turbulence at high friction Reynolds numbers, *Physical Review Fluids* **7**, 014602 (2022).
- [11] A. Liakopoulos and A. Palasis, Turbulent Channel Flow: Direct Numerical Simulation-Data-Driven Modeling, *Fluids* **9**, 62 (2024).
- [12] B. Kader, Temperature and concentration profiles in fully turbulent boundary layers, *International Journal of Heat and Mass Transfer* **24**, 1541 (1981).
- [13] C. Carvin, J. Debieve, and A. Smits, The near-wall temperature profile of turbulent boundary layers, in *26th Aerospace Sciences Meeting* (American Institute of Aeronautics and Astronautics, Reno, NV, U.S.A., 1988).
- [14] J. Lee, S. Y. Jung, H. J. Sung, and T. A. Zaki, Turbulent thermal boundary layers with temperature-dependent viscosity, *International Journal of Heat and Fluid Flow* **49**, 43 (2014).
- [15] S. Pirozzoli, M. Bernardini, and P. Orlandi, Passive scalars in turbulent channel flow at high Reynolds number, *Journal of Fluid Mechanics* **788**, 614 (2016).
- [16] F. Alcántara-Ávila, S. Hoyas, and M. Jezabel Pérez-Quiles, Direct numerical simulation of thermal channel flow for $Re\tau=5000$ and $Pr=0.71$, *Journal of Fluid Mechanics* **916**, 10.1017/jfm.2021.231 (2021).
- [17] M. V. Morkovin, Effects of compressibility on turbulent flows, in *Mécanique de la Turbulence*, edited by A. Favre (CNRS, 1962) pp. 367–380.
- [18] E. R. Van Driest, Turbulent boundary layer in compressible fluids, *Journal of the Aeronautical Sci-*

ences **18**, 145 (1951).

[19] Y.-S. Zhang, W.-T. Bi, F. Hussain, X.-L. Li, and Z.-S. She, Mach-Number-Invariant Mean-Velocity Profile of Compressible Turbulent Boundary Layers, *Physical Review Letters* **109**, 054502 (2012).

[20] C. Brun, M. Petrovan Boiarcicu, M. Haberkorn, and P. Comte, Large eddy simulation of compressible channel flow: Arguments in favour of universality of compressible turbulent wall bounded flows, *Theoretical and Computational Fluid Dynamics* **22**, 189 (2008).

[21] A. Trettel and J. Larsson, Mean velocity scaling for compressible wall turbulence with heat transfer, *Physics of Fluids* **28**, 026102 (2016).

[22] A. Patel, B. J. Boersma, and R. Pecnik, The influence of near-wall density and viscosity gradients on turbulence in channel flows, *Journal of Fluid Mechanics* **809**, 793 (2016).

[23] K. P. Griffin, L. Fu, and P. Moin, Velocity transformation for compressible wall-bounded turbulent flows with and without heat transfer, *Proceedings of the National Academy of Sciences* **118**, e2111144118 (2021).

[24] P. S. Volpiani, P. S. Iyer, S. Pirozzoli, and J. Larsson, Data-driven compressibility transformation for turbulent wall layers, *Physical Review Fluids* **5**, 052602 (2020).

[25] H. Lee, C. Helm, P. M. Martín, and O. J. H. Williams, Compressible boundary layer velocity transformation based on a generalized form of the total stress, *Physical Review Fluids* **8**, 074604 (2023).

[26] K. Younes and J.-P. Hickey, Mean velocity scaling of high-speed turbulent flows under nonadiabatic wall conditions, *AIAA Journal* **61**, 1532 (2023), <https://doi.org/10.2514/1.J062547>.

[27] L. Crocco, Sulla trasmissione del calore da una lamina piana a un fluido scorrente ad alta velocità, *LAerotecnica* **12**, 181 (1932).

[28] A. Busemann, *Handbuch der Experimentalphysik*, 4 (Geest und Port, 1931).

[29] A. Walz, Compressible turbulent boundary layers, in *CNRS Publication* (CNRS, 1962) pp. 299–350.

[30] L. Duan and M. P. Martín, Direct numerical simulation of hypersonic turbulent boundary layers. Part 4. Effect of high enthalpy, *Journal of Fluid Mechanics* **684**, 25 (2011).

[31] Y.-S. Zhang, W.-T. Bi, F. Hussain, and Z.-S. She, A generalized Reynolds analogy for compressible wall-bounded turbulent flows, *Journal of Fluid Mechanics* **739**, 392 (2014).

[32] C. Cheng and L. Fu, A Reynolds analogy model for compressible wall turbulence, *Journal of Fluid Mechanics* **999**, A20 (2024).

[33] D. Modesti and S. Pirozzoli, Reynolds and Mach number effects in compressible turbulent channel flow, *International Journal of Heat and Fluid Flow* **59**, 33 (2016).

[34] L. Duan, I. Beekman, and M. P. Martín, Direct numerical simulation of hypersonic turbulent boundary layers. Part 2. Effect of wall temperature, *Journal of Fluid Mechanics* **655**, 419 (2010).

[35] C. Cheng and L. Fu, Mean temperature scalings in compressible wall turbulence, *Physical Review Fluids* **9**, 054610 (2024).

[36] X. Chen, J. Gan, and L. Fu, Mean temperature–velocity relation and a new temperature wall model for compressible laminar and turbulent flows, *Journal of Fluid Mechanics* **1009**, A39 (2025).

[37] Y. Song, P. Zhang, Y. Liu, and Z. Xia, Central mean temperature scaling in compressible turbulent channel flows with symmetric isothermal boundaries, *Physical Review Fluids* **7**, 044606 (2022).

[38] D. J. Lusher and G. N. Coleman, Numerical Study of Compressible Wall-Bounded Turbulence – the Effect of Thermal Wall Conditions on the Turbulent Prandtl Number in the Low-Supersonic Regime, *International Journal of Computational Fluid Dynamics* **36**, 797 (2022).

[39] D. Coles, The law of the wake in the turbulent boundary layer, *Journal of Fluid Mechanics* **1**, 191 (1956).

[40] P. G. Huang and G. N. Coleman, Van Driest transformation and compressible wall-bounded flows, *AIAA Journal* **32**, 2110 (1994).

[41] A. Patel, B. J. Boersma, and R. Pecnik, Scalar statistics in variable property turbulent channel flows, *Physical Review Fluids* **2**, 084604 (2017).

[42] P. E. Chen, G. P. Huang, Y. Shi, X. I. Yang, and Y. Lv, A unified temperature transformation for high-Mach-number flows above adiabatic and isothermal walls, *Journal of Fluid Mechanics* **951**, A38 (2022).

[43] D. Modesti and S. Pirozzoli, Friction and heat transfer in forced air convection with variable physical properties, *Journal of Fluid Mechanics* **1001**, A27 (2024).

[44] S. Pirozzoli, Revisiting the mixing-length hypothesis in the outer part of turbulent wall layers: Mean flow and wall friction, *Journal of Fluid Mechanics* **745**, 378 (2014).

[45] D. Wilcox, *Turbulence Modeling for CFD*, Turbulence Modeling for CFD No. Bd. 1 (DCW Industries, 2006).

[46] P. Luchini, Universality of the Turbulent Velocity Profile, *Physical Review Letters* **118**, 224501 (2017).

[47] P. G. Huang, G. N. Coleman, and P. Bradshaw, Compressible turbulent channel flows: DNS results and modelling, *Journal of Fluid Mechanics* **305**, 185 (1995).

[48] X. Zhu, Y. Song, P. Zhang, X. Yang, Y. Ji, and Z. Xia, Influences of streamwise driving forces on turbulent statistics in direct numerical simulations of compressible turbulent channel flows, *Physical*

Review Fluids **10**, 064616 (2025).

- [49] J. Guo, X. Yang, and M. Ihme, Structure of the thermal boundary layer in turbulent channel flows at transcritical conditions, *Journal of Fluid Mechanics* **934**, A45 (2022).
- [50] A. M. Hasan, J. Larsson, S. Pirozzoli, and R. Pecnik, Incorporating intrinsic compressibility effects in velocity transformations for wall-bounded turbulent flows, *Physical Review Fluids* **8**, L112601 (2023).
- [51] J. Larsson, S. Kawai, J. Bodart, and I. Bermejo-Moreno, Large eddy simulation with modeled wall-stress: Recent progress and future directions, *Mechanical Engineering Reviews* **3**, 15 (2016).
- [52] X. I. A. Yang and Y. Lv, A semi-locally scaled eddy viscosity formulation for LES wall models and flows at high speeds, *Theoretical and Computational Fluid Dynamics* **32**, 617 (2018).
- [53] Z.-S. She, X. Chen, and F. Hussain, Quantifying wall turbulence via a symmetry approach: A Lie group theory, *Journal of Fluid Mechanics* **827**, 322 (2017).
- [54] S. Kundu, M. Kumbhakar, and K. Ghoshal, Reinvestigation on mixing length in an open channel turbulent flow, *Acta Geophysica* **66**, 93 (2018).
- [55] Y. Xu, S. J. Schmidt, and N. A. Adams, Extending the logarithmic velocity profile in turbulent channel flow, *Physics of Fluids* **37**, 045109 (2025).
- [56] X. Zhu, Y. Song, X. Yang, and Z. Xia, Velocity transformation for compressible wall-bounded turbulence—An approach through the mixing length hypothesis, *Science China Physics, Mechanics & Astronomy* **67**, 294711 (2024).
- [57] E. R. Van Driest, On Turbulent Flow Near a Wall, *Journal of the Aeronautical Sciences* **23**, 1007 (1956).
- [58] K. P. Griffin, L. Fu, and P. Moin, Near-wall model for compressible turbulent boundary layers based on an inverse velocity transformation, *Journal of Fluid Mechanics* **970**, A36 (2023).
- [59] H. M. Nagib and K. A. Chauhan, Variations of von Kármán coefficient in canonical flows, *Physics of Fluids* **20**, 101518 (2008).
- [60] G. Gerolymos and I. Vallet, Scaling of pressure fluctuations in compressible turbulent plane channel flow, *Journal of Fluid Mechanics* **958**, A19 (2023).
- [61] G. Gerolymos and I. Vallet, Compressible turbulent plane channel DNS datasets, *Data in Brief* **55**, 110737 (2024).
- [62] G. Gerolymos and I. Vallet, Total and static temperature statistics in compressible turbulent plane channel flow, *Journal of Fluid Mechanics* **978**, A25 (2024).
- [63] G. Gerolymos and I. Vallet, Pressure, density, temperature and entropy fluctuations in compressible

turbulent plane channel flow, *Journal of Fluid Mechanics* **757**, 701 (2014).

[64] D. A. Bezgin, A. B. Buhendwa, and N. A. Adams, JAX-Fluids: A fully-differentiable high-order computational fluid dynamics solver for compressible two-phase flows, *Computer Physics Communications* **282**, 108527 (2023).

[65] D. A. Bezgin, A. B. Buhendwa, and N. A. Adams, JAX-Fluids 2.0: Towards HPC for differentiable CFD of compressible two-phase flows, *Computer Physics Communications* **308**, 109433 (2025).

[66] D. A. Bezgin, A. B. Buhendwa, S. J. Schmidt, and N. A. Adams, ML-ILES: End-to-end optimization of data-driven high-order Godunov-type finite-volume schemes for compressible homogeneous isotropic turbulence, *Journal of Computational Physics* **522**, 113560 (2025).

[67] N. Adams, S. Hickel, and S. Franz, Implicit subgrid-scale modeling by adaptive deconvolution, *Journal of Computational Physics* **200**, 412 (2004).

[68] S. Hickel and N. A. Adams, On implicit subgrid-scale modeling in wall-bounded flows, *Physics of Fluids* **19**, 105106 (2007).

[69] S. Hickel, C. P. Egerer, and J. Larsson, Subgrid-scale modeling for implicit large eddy simulation of compressible flows and shock-turbulence interaction, *Physics of Fluids* **26**, 106101 (2014).

[70] M. Bernardini, S. Pirozzoli, and P. Orlandi, Velocity statistics in turbulent channel flow up to $Re\tau=4000$, *Journal of Fluid Mechanics* **742**, 171 (2014).

[71] G. N. Coleman, J. Kim, and R. D. Moser, A numerical study of turbulent supersonic isothermal-wall channel flow, *Journal of Fluid Mechanics* **305**, 159 (1995).

[72] L. Duan, I. Beekman, and M. P. Martín, Direct numerical simulation of hypersonic turbulent boundary layers. Part 3. Effect of Mach number, *Journal of Fluid Mechanics* **672**, 245 (2011).

[73] M. Cogo, F. Salvadore, F. Picano, and M. Bernardini, Direct numerical simulation of supersonic and hypersonic turbulent boundary layers at moderate-high Reynolds numbers and isothermal wall condition, *Journal of Fluid Mechanics* **945**, A30 (2022).

[74] J. Yao and F. Hussain, Turbulence statistics and coherent structures in compressible channel flow, *Physical Review Fluids* **5**, 084603 (2020).

[75] S. T. Bose and G. I. Park, Wall-Modeled Large-Eddy Simulation for Complex Turbulent Flows, *Annual Review of Fluid Mechanics* **50**, 535 (2018).

[76] T. R. Hendrickson, P. Subbareddy, and G. V. Candler, Improving Eddy Viscosity Based Turbulence Models for High Speed, Cold Wall Flows, in *AIAA SCITECH 2022 Forum* (American Institute of Aeronautics and Astronautics, San Diego, CA & Virtual, 2022).

[77] T. R. Hendrickson, P. Subbareddy, G. V. Candler, and R. L. Macdonald, Applying compressible transformations to wall modeled LES of cold wall flat plate boundary layers, in *AIAA SCITECH 2023 Forum* (American Institute of Aeronautics and Astronautics, National Harbor, MD & Online, 2023).

[78] U. Schumann, Subgrid scale model for finite difference simulations of turbulent flows in plane channels and annuli, *Journal of Computational Physics* **18**, 376 (1975).

[79] G. Groetzbach, Direct numerical and large eddy simulation of turbulent channel flows, in *Encyclopedia of Fluid Mechanics*, edited by N. Cheremisinoff (Gulf Publishing, West Orange, NJ, 1987) pp. 1337–1391.

[80] U. Piomelli, J. Ferziger, P. Moin, and J. Kim, New approximate boundary conditions for large eddy simulations of wall-bounded flows, *Physics of Fluids A: Fluid Dynamics* **1**, 1061 (1989).

[81] U. Piomelli and E. Balaras, Wall-layer models for large-eddy simulations, *Annual Review of Fluid Mechanics* **34**, 349 (2002).

[82] F. Nicoud, J. S. Baggett, P. Moin, and W. Cabot, Large eddy simulation wall-modeling based on suboptimal control theory and linear stochastic estimation, *Physics of Fluids* **13**, 2968 (2001).

[83] J. A. Templeton, M. Wang, and P. Moin, An efficient wall model for large-eddy simulation based on optimal control theory, *Physics of Fluids* **18**, 025101 (2006).

[84] S. Pirozzoli, An explicit representation for mean profiles and fluxes in forced passive scalar convection, *Journal of Fluid Mechanics* **968**, R1 (2023).

[85] S. Pirozzoli and D. Modesti, Mean temperature profiles in turbulent internal flows, *International Journal of Heat and Fluid Flow* **109**, 109544 (2024).

[86] C.-C. Sun and M. E. Childs, A modified wall wake velocity profile for turbulent compressible boundary layers., *Journal of Aircraft* **10**, 381 (1973).

[87] X. Chen and Z.-S. She, Analytic prediction for planar turbulent boundary layers, *Science China Physics, Mechanics & Astronomy* **59**, 114711 (2016).

[88] C. Zhang, L. Duan, and M. M. Choudhari, Direct Numerical Simulation Database for Supersonic and Hypersonic Turbulent Boundary Layers, *AIAA Journal* **56**, 4297 (2018).

[89] L. Szajnecki, D. Roy, L. Duan, and N. J. Bisek, Effect of Reynolds number on a high-speed cold-wall turbulent boundary layer, *Journal of Fluid Mechanics* **1016**, A49 (2025).